

Iterative reconstruction methods for rosette trajectories in functional MRI

by
Sangwoo Lee

A thesis submitted in partial fulfillment
of the requirements for the degree of
Doctor of Philosophy
(Electrical Engineering and Computer Science)
in The University of Michigan
2006

Doctoral Committee:

Professor Douglas C. Noll, Co-chair
Professor Jeffrey A. Fessler, Co-chair
Professor Alfred O. Hero III
Professor Thomas L. Chenevert



© SangwooLee 2006
All Rights Reserved

To Una

ACKNOWLEDGEMENTS

First of all, I would like to thank my advisors, Professor Douglas C. Noll and Professor Jeffrey A. Fessler. Their guidance has been the most powerful, and the most effective way to motivate myself throughout the PhD work, which sometimes turns out to be a very difficult period of one's life. There were many let-down moments due to various reasons in my life, but they have always given me thoughtful and considerate advice. I thank you both for all the help! I would like to thank my other committee members, Professor Alfred O. Hero III and Professor Thomas L. Chenevert for their valuable input to my thesis.

This work could not be finished without the help of fMRI lab people. I thank ChunYu Yip for being a wonderful friend and also inspiring me for many research projects. I thank Scott Peltier and Alberto Vazquez for providing all the helps and bearing with all the basic questions I asked when I first came to the lab. I thank Luis Hernandez for instructions on many functional MRI data analysis stuffs, and also being a good friend. I thank Brad Sutton and Valur Olafsson for many insightful discussions, suggestions and helps on the image reconstruction problems. I thank Greg Lee for his ubiquitous help on pulse sequence programming. I thank Kiran Pandey for bringing in the new culture of celebrating everyone's birthday. It was a wonderful thing to do, and I enjoyed the cakes! I thank YoonChung Kim for many valuable discussions on parallel imaging. I thank Bryan Donald, Sumati Krishnan, Will Grissom, Eve Gochis, Keith Newnham for their invaluable helps in many things.

The years in Ann Arbor also helped me discover the deep love of family I was given. I thank my parents. They have been very patient with me, and encouraging all the time. I thank my sister and Shri. Their guidance and help always gave me fuel to go farther than I could. My only wife, Una, you have been such a wonderful wife for me throughout the past years. We have gone through a lot of things in Ann Arbor, and I wish we can finish our blessed journey together for the rest of my life. I really thank you for being patient with me, and giving endless love to give the real reason for me to wake up every morning. I also thank Kristin for being such a wonderful child. I never imagined to have such an adorable daughter in my life. I wish I can get more and more love to show you in the remaining time allowed for us.

Finally, I thank God for bringing me into this wonderful world and wonderful people. I did not deserve to be given any of these, but you gave priceless things for no price.

TABLE OF CONTENTS

DEDICATION	ii
ACKNOWLEDGEMENTS	iii
LIST OF TABLES	vii
LIST OF FIGURES	viii
CHAPTER	
I. Introduction	1
1.1 Background	4
II. Iterative Reconstruction for SMART Imaging	27
2.1 Introduction	27
2.2 Theory	30
2.3 Methods	35
2.4 Results	41
2.5 Discussion	46
2.6 Conclusion	50
III. A robust, dynamic R_2^*-and-field-map-corrected image reconstruction for single shot self-refocusing trajectories at 3T	52
3.1 Introduction	52
3.2 Theory	55
3.3 Simulations	63
3.4 Experiments	68
3.5 Discussion	73
3.6 Conclusion	77
IV. 2D k-space trajectory measurement	78
4.1 Introduction	78
4.2 Methods	79
4.3 Results	84
4.4 Discussions and Conclusions	88
V. Conclusions and future work	90
5.1 Conclusion	90
5.2 Future work	92

BIBLIOGRAPHY 96



LIST OF TABLES

Table

1.1	Average T_1 , T_2 , and T_2^* values found in human brain at 3 T [1].	6
2.1	Simulation result : NRMSE of the reconstructed images. NRMSE was measured in the support illustrated in figure 2.4.	42
3.1	Estimation errors of the field maps and R_2^* maps for synthesized data sets with different field map magnitudes. Field map 3 (max amplitude = 79.1 Hz) is identical to the reference field map shown in Fig. 3.4. Field maps 1 (max amplitude = 26.4 Hz) and 2 (max amplitude = 52.7 Hz) are obtained by scaling field map 3 by 0.33 and 0.67, respectively.	68
4.1	Delays of the measured trajectory with respect to the designed trajectory ($4 \mu s$ sampling time)	85

LIST OF FIGURES

Figure

1.1	Spinwarp acquisition is done by acquiring one line in the 2D k-space after each RF excitation. TR denotes the <i>repetition time</i> , which is the time between RF excitations.	8
1.2	(a) Echo Planar Imaging (EPI) trajectory. (b) Spiral trajectory.	9
1.3	(a) A rosette trajectory with $\omega_1=1042$ Hz, $\omega_2=22$ Hz, max slew = 156 mT/m/ms, max gradient = 2.38 G/cm. (b) A rosette trajectory with $\omega_1=1087$ Hz, $\omega_2=113$ Hz, max slew = 171 mT/m/ms, max gradient = 2.38 G/cm.	12
1.4	(a) Spectral selectivity of the rosette trajectory shown in figure 1.3 (a). This trajectory results in off-resonance artifacts around the edges of the simulation object. The images were reconstructed without off-resonance correction, where the k-space data was modulated by the off-resonance frequencies (0 Hz, 75 Hz, 150 Hz, 225 Hz) indicated by the arrows. (b) Spectral selectivity of the rosette trajectory shown in figure 1.3 (b). Unlike the previous example, this trajectory has very good suppression of the simulation object at nonzero off-resonance locations.	15
1.5	Pulse sequence for SMART imaging. The pulse sequence is very similar to the conventional single shot gradient echo imaging sequence except for the SMART gradient and the multi-slice excitation RF pulse.	17
1.6	Figure 5 of [2]. "Comparison of single-slice rosette acquisition (a-c) and triple-slice SMART acquisition (d-l) for experimental data acquired using the single-shot rosette trajectory. Images are presented for the average control condition (a,d,g,j), the average active condition (b,e,h,k), and the average difference (x 60) of active and control conditions (c,f,i,l). Activation areas are marked with arrows" [2]. Note that this experiment was performed using 1.5 T scanner, and the in-plane spatial resolution was kept to 5 mm to accommodate the hardware limitations (max slew rate 120 mT/m/ms).	18
2.1	(a) Diagram of SMART method. Three slices at locations z_1 , z_2 , and z_3 are excited simultaneously. During the readout, a linear gradient in slice-select direction is played to introduce spatially constant off-resonance at each slice location. (b) Pulse sequence of SMART acquisition	29
2.2	An example of a SMART acquisition to cover a 3D volume. Slices 1A,2A,3A are simultaneously excited, and the excitation of slices 1B,2B,3B and 1C,2C,3C follow. In order to fill up the space without a gap, the center-to-center slice distance should be one third of the thickness of the 3D volume. Only the slices in the dashed box need to be prescribed in the scanner.	30
2.3	(a) Rosette trajectory. (b) Spectral selectivity of the rosette trajectory in (a). . . .	35

2.4	(a)-(c) The reference images used in the simulation. (d)-(f) The reference field maps used in the simulation overlaid with the support of the reference images.	36
2.5	Simulation results : (a) the reference discrete object (b) the conjugate phase reconstruction (c) the iterative single slice reconstruction (d) the proposed iterative SMART reconstruction	41
2.6	NRMSE of each reconstruction methods. The error was measured inside of the object. (a) slice 1 (b) slice 2 (c) slice 3	42
2.7	Sensitivity of each reconstruction method to the field map errors	44
2.8	(a) The FWHM of the point spread function of each reconstruction method. Center profiles of the point spread functions of the on-resonant slice (slice 2) and the off-resonant slices (slice 1 and 3): (b) conjugate phase (CPSMART) reconstruction (c) iterative single slice (ssiSMART) reconstruction (d) iterative SMART (iSMART) reconstruction.	45
2.9	(a) Reconstructed images from a single slice acquisition. (b) CPSMART reconstructed images from SMART acquisition. (c) ssiSMART reconstructed images from SMART acquisition. (d) iSMART reconstructed images from SMART acquisition.	46
2.10	(a) Activation maps from single slice acquisition. (b) Activation maps from CPSMART reconstruction of SMART acquisition. (c) Activation maps from ssiSMART reconstruction of SMART acquisition. (d) Activation maps from iSMART reconstruction of SMART acquisition.	47
2.11	The number of activated pixels for each slice ($p=0.05$). Slice 1 denotes the superior side of the imaging volume.	47
3.1	(a) Single shot PR trajectory (sequential view ordering) (b) single shot rosette trajectory (c) single shot PR pulse sequence (d) single shot rosette sequence	55
3.2	The proposed R_2^* corrected reconstruction scheme (dotted line) and dynamic R_2^* estimation (solid line)	57
3.3	(a) The reference field map. (b) Estimated field map from conventional 'two-point' method (RMSE = 14.23Hz, Max error = 98.5Hz). (c) Estimated field map from the proposed field map estimation method (RMSE = 3.43Hz, Max error = 34.46Hz).	62
3.4	The reference image (a), R_2^* map (b), and field map (c) used in simulations	63
3.5	The minimum NRMSE of subimages with different β and γ values for various data lengths and numbers of segments.	65
3.6	(a) Field-map-corrected image using the reference field map without R_2^* correction (NRMSE=0.28), (b) field-map-corrected T_2^* -weighted image using the initial field map without R_2^* correction (NRMSE=0.31), (c) proposed method with the initial field map (16th subimage, NRMSE=0.064), (d) proposed method with the reference field map (16th subimage, NRMSE=0.042). (e) The NRMSE of each subimage for (c) and (d). The maximum error in the initial field map was 47.9Hz with RMSE of 3.1Hz. The design parameters for the proposed method were $\beta=1$, $\gamma=400$, $L=32$	67

3.7	(a) (f) The subimages ($l=1,5,9,13,17,21$) and their profiles. (g) the estimated R_2^* map (RMSE = $1.32sec^{-1}$) and (h) the estimated field map (RMSE = $0.52Hz$).	68
3.8	Experiment I : The 24 reconstructed subimages from a single shot gradient echo rosette data set (readout = $44.4ms$). The left top image is the first subimage.	71
3.9	Experiment I : (a) Image without field map correction. (b) Field-map-corrected T_2^* -weighted image reconstructed from standard iterative reconstruction. (c) Proposed R_2^* -and-field-map-corrected reconstruction (12th subimage in Figure 3.8). In (b) and (c), the initial field map, which was estimated using the method described in section 3.2.5, was used in the reconstructions.	72
3.10	Experiment II : The estimated R_2^* map and field map from the proposed R_2^* -and-field-map estimation method.	72
3.11	Experiment II : Activation maps (left) and the corresponding averaged time course of the activated pixels (right). (a) The dynamic R_2^* maps from the proposed R_2^* -and-field-map-estimation method. (b) The 24th subimages from the proposed R_2^* -and-field-map-estimation method. (c) The field-map-corrected T_2^* -weighted images with static field map estimated from the first time point. (d) The dynamic field-map-corrected T_2^* -weighted images, where dynamic field maps were estimated from the proposed R_2^* -and-field-map-estimation method.	74
3.12	Experiment II : (a) The normalized mean time series of the four experiments from Fig. 3.11. Each line represents the time series of the R_2^* maps from the proposed R_2^* -and-field-map estimation method (1), the 24th subimages from the proposed R_2^* -and-field-map estimation method (2), the field-map-corrected T_2^* -weighted images using the field map estimated from the first time point (3), and the dynamic field-map-corrected T_2^* -weighted images using the field maps estimated from the proposed R_2^* -and-field-map-estimation method (4). (b) The average time course of the dynamic field map estimated using the proposed R_2^* -and-field-map-estimation method.	75
4.1	(a) Illustration of a pencil excitation at $(X_0, 0)$. (b) The pulse sequence used to measure $k_x(t)$. (c) The proposed k-space trajectory measurement scheme	81
4.2	(a) The measured trajectory and the designed trajectory for the first half (spiral in) of the spiral in-out trajectory (b) The measured trajectory and the designed trajectory for the second half (spiral out) of the spiral in-out trajectory (c) The measured phase accumulation from B_0 fluctuation, $\phi_0(t)$	84
4.3	The cross coupling of the gradient channels was measured by setting the amplitude of the X readout gradient as 0, and measuring $k_x(t)$ while the other channel was on using the proposed measurement method.	85
4.4	The images reconstructed from spiral in-out data in the human experiment. (a) The designed k-space trajectory was used for the reconstruction. (b) The measured trajectory was used for the reconstruction. The arrows indicate reduction of the reconstruction artifacts when the measured trajectory was used.	86

4.5 Simulation results using the measured k-space trajectory and B_0 fluctuation. The k-space data was synthesized using the measured k-space trajectory and $\phi_0(t)$, then reconstruction was done by incorporating the following variations into the reconstruction system model. (a) The reference reconstruction : The measured k-space trajectory and $\phi_0(t)$, (b) Difference map between the reference reconstruction and the magnitude image using the designed k-space trajectory with $\phi_0(t)$ (NRMSE=0.0534), (c) Difference map between the reference reconstruction and the magnitude image using the measured k-space trajectory without $\phi_0(t)$ (NRMSE=0.0114), (d) Difference map between the reference reconstruction and the magnitude image using the designed k-space trajectory without $\phi_0(t)$ (NRMSE=0.0534). All difference maps were scaled by 22 for visualization purpose. The NRMSE were measured with respect to the reference reconstruction (a) inside of the object. 87

CHAPTER I

Introduction

Functional MRI (Magnetic Resonance Imaging) is a noninvasive imaging method to explore the function of the human brain, both in normal subjects and in clinical populations. In most fMRI (functional MRI) studies, brain function mapped from a set of MR images of a subject with a controlled manipulation of a task or stimulus. However, while current methods have been used to provide valuable information about structure and functional relationships, there still are limitations in temporal and spatial resolution not to mention those from the artifacts of the reconstructed images.

There has been remarkable progress for fast 2D functional imaging methods both in temporal and spatial resolution. However, whole brain imaging is still a challenging problem, since it requires excessive data acquisition in much larger volumes of interest than several slices. Acquisition of the entire brain is desirable because the human brain is organized in a distributed fashion with many different regions involved in performing even very simple tasks. For example, the neural circuitry involved in motor function includes primary sensory and motor cortices (bilateral precentral gyrus), supplementary motor area (midline frontal cortex), higher motor planning areas (anterior prefrontal cortex), cerebellum, striatum, and other sub-cortical areas.

In addition, the fidelity of movement correction in transverse and through-plane directions depends on large volumes of acquisition.

In work by Savoy, et al. [3], consistency in the response between hemispheres in visual cortex allowed stimulus timing differences of 500 ms to be detected. This sets a goal for the temporal resolution for only a single location to detect a single response. In conventional fast single-shot techniques such as EPI (Echo Planar Imaging) and spiral imaging, for distributed locations to be imaged with adequate spatial and temporal resolution, the scan time should increase as the number of locations to be imaged is increased. In MRI, samples of the Fourier transform of an image are acquired and the image is reconstructed using the inverse Fourier Transform or equivalent operation. Those single-shot methods have a limitation that they can image only one slice at one time.

To increase the temporal resolution for multi-locations, SMART (Simultaneous Multi-slice Acquisition using Rosette Trajectories) was suggested by Noll [2] in 1.5T, in which data points are acquired from multiple slices simultaneously, then each image is reconstructed after demodulating the data at the resonant frequency of each slice. However, the originally proposed image reconstruction scheme (conjugate phase reconstruction) introduced the artifacts from the off-resonance slices. Even though these artifacts were shown to be mostly stationary, the artifacts hamper proper motion correction of each image for functional studies, and the effect of physiological signal on the artifacts from the off-resonance slices were not clearly understood. The artifacts also limit the use of SMART method to only functional MRI where dynamic information is most important.

The principal objective of this work was to develop a reconstruction method for SMART imaging for reduced off-resonance artifact, and implement SMART in a

3 T scanner. To reduce the artifacts from off-resonance slices, we developed an iterative reconstruction method for SMART acquisition. The SMART acquisition was implemented in our 3T scanner, and the results of simulations and functional experiment are presented in chapter II.

Imaging at a higher field strength is desirable, since in general, higher magnetic field results in higher MR signal to noise ratio. However, as we implemented the SMART acquisition in a 3T scanner, we faced more difficulties than in 1.5 T due to the increased susceptibility induced off-resonance, and the relatively less effective gradient shimming system. In fact, the increased off-resonance not only affected SMART imaging, but also conventional single slice imaging using rosette trajectory. The off-resonance effect will be more problematic at even higher fields such as 7T.

On the other hand, iterative reconstruction for SMART or conventional single slice imaging is found to be more sensitive to errors in the MR system model, e.g. field map errors than non-iterative conjugate phase reconstruction. Therefore, it was essential to estimate a very accurate off-resonance map for iterative field-map corrected image reconstruction methods. One would increase the number of shots in the conventional two-echo field map measurement method, but this method is limited by extended scan time opening the door to the additional field map error from respiration, motion and scanner drift.

To reconstruct images from field maps with limited accuracy, and also to estimate field maps with higher accuracy, we proposed a spatio-temporally regularized iterative reconstruction method for single slice rosette imaging in chapter III. Using this method, we can estimate a very accurate field map as well as dynamic field-map corrected images and the R_2^* maps. Simulation and a functional imaging results are shown.

Dynamic R_2^* mapping can be another useful tool for functional MRI, since it provides nearly optimal contrast to noise ratio without prior knowledge of the tissue T_2^* , and also R_2^* can serve as a more physiologically related parameter for inter- and intra- subject comparisons between functional studies.

In chapter IV, we propose another approach to improve the accuracy of the system model for the iterative reconstruction. In this method, we use a pencil excitation to accurately estimate the actual k-space trajectory and also the fluctuation of main magnetic field during the data acquisition. Chapter V will contain the conclusion, the list of the contributions of this thesis, and the future work.

We start with the brief overview of background materials such as MRI physics, SMART imaging, and image reconstruction methods for non-Cartesian k-space trajectories in the following sections.

1.1 Background

1.1.1 MRI Physics

Magnetic resonance imaging (MRI) is based on the quantum mechanical property of nuclear spin. Nuclei having an odd number of neutrons, odd number of protons, or both possess a net nuclear spin angular momentum and magnetic moment, therefore exhibiting the MR phenomenon. Classically, these nuclei can be visualized as spinning charged spheres that give rise to a small magnetic moment. These MR-active nuclei are referred to as simply *spins*. In biological specimens, hydrogen (1H), with a single proton, is the most abundant (mostly from H_2O), the most sensitive, and by far the most studied element. In MRI experiment, the object to be imaged is placed into a large, static magnetic field, \vec{B}_0 . The magnetic moments associated with nuclear spin tend to align themselves parallel or anti-parallel to \vec{B}_0 . Therefore,

the resultant macroscopic net magnetization \vec{M} is formed parallel to \vec{B}_0 .

The magnetization demonstrates a resonance phenomenon at a characteristic frequency determined by the Larmor relationship,

$$(1.1) \quad \omega_0 = \gamma B_0$$

where B_0 is the strength of the main magnetic field, and γ is a constant unique for each isotope and called as the gyromagnetic ratio with $\frac{\gamma}{2\pi} = 42.58 \text{ MHz/Tesla}$ for ^1H . Therefore, the magnetization can be perturbed by applying an oscillating magnetic field \vec{B}_1 at this resonance frequency. This process is called excitation, and the magnetization is partially or completely tipped into the plane perpendicular to the main magnetic field \vec{B}_0 forming a detectable state of magnetic spins. Once excited, the magnetization precesses around the static magnetic field at its resonant frequency given in equation (1.1). A coil placed near to the object can detect this precessing magnetization. Therefore, the received signal can be expressed as the total signal from excited (precessing) magnetization.

The excited magnetization is governed by the Bloch equation

$$(1.2) \quad \frac{dM}{dt} = M \times \gamma B - \frac{M_x \vec{i} + M_y \vec{j}}{T_2} - \frac{(M_z - M_0) \vec{k}}{T_1},$$

where M_x and M_y are the transverse component of the magnetization, M_z is the longitudinal component of the magnetization and T_2 and T_1 are transverse and longitudinal relaxation constants. In MR signal equation derived from equation (1.2), T_2 is often replaced by T_2^* . T_2^* is composed of two components as $1/T_2^* = 1/T_2' + 1/T_2$, where T_2' is time constant for a *recoverable* spin dephasing due to the macroscopic field inhomogeneities, and T_2 is the *spin-spin relaxation* constant, which is due to dynamic variations in the local precessional frequencies. Table (1.1.1) shows typical values of T_2 , T_1 , and T_2^* of human brain tissues at 3T.

	T_1 (msec, \pm SE)	T_2 (msec, \pm SE)	T_2^* (msec, \pm SE)
White matter	832 ± 10	79.6 ± 0.6	44.7 ± 1.2 (frontal) 48.4 ± 4.5 (occipital)
Gray matter	1331 ± 13	110 ± 2	51.8 ± 3.3 (frontal) 41.6 ± 2.0 (occipital)

Table 1.1: Average T_1 , T_2 , and T_2^* values found in human brain at 3 T [1].

Once the magnetization is tipped onto the transverse plane after RF excitation, the precessing transverse component of $M(\vec{r}, t)$ goes through T_2^* exponential decay. As spatially encoding gradients are played during the readout, the received signal is integration of the signals from the transverse magnetizations in the imaging volume, which go through phase evolution and magnitude change as

$$\begin{aligned}
 (1.3) \quad S_r(t) &= \int_{vol} M(\vec{r}, t) dV + \varepsilon(t) \\
 &= \int_{vol} M_0(\vec{r}) e^{-i\gamma B_0 t} e^{-i\omega_0(\vec{r})t} e^{-t/T_2^*(\vec{r})} e^{-i\gamma \int_0^t \vec{G}(\tau) \cdot \vec{r} d\tau} d\vec{r} + \varepsilon(t),
 \end{aligned}$$

where γB_0 is the global precession frequency dictated by the Larmor relation, $\omega_0(\vec{r})$ is spatially varying off-resonance caused by local field inhomogeneity, \vec{G} is the spatially encoding gradient, $\varepsilon(t)$ denotes noise, and \vec{r} denotes the spatial locations. Note that this signal equation ignores constant gain factors and constant phase factors, and assumes uniform sensitivity of receiving coils in the region of interest.

The off-resonance $\omega_0(\vec{r})$ is caused by the local disturbance of the magnetic field from spatial distribution of magnetic susceptibility in the imaging object. The primary source of the noise in MR system is considered to be the electrical random fluctuation caused by the Brownian motion of electrons in the receiver coil and the imaging object [4]. This noise is added to the raw received signal and goes through the quadrature detection-demodulation to result in an additive bi-variate white Gaussian noise.

Demodulating the received signal at the Larmor frequency and using the k -space

notation, the baseband received signal is

$$(1.4) \quad S_r(t) = \int_{vol} M_0(\vec{r}) e^{-t/T_2^*(\vec{r})} e^{-i\omega_0(\vec{r})} e^{-i2\pi\vec{k}(t)\cdot\vec{r}} d\vec{r} + \varepsilon(t),$$

where $\vec{k}(t) \triangleq \frac{\gamma}{2\pi} \int_0^t \vec{G}(\tau) d\tau.$

Ignoring the phase evolution from $\omega_0(\vec{r})$ and T_2^* decay, the *k-space* term $\vec{k}(t)$ in equation (1.4) is a trajectory traversed in time in a three dimensional Fourier space of $M_0(\vec{r})$. The goal of MR image reconstruction is restoration of $M_0(\vec{r})$ from the samples of the received signal $S_r(t)$, and the choice of a k-space trajectory determines imaging parameters such as the size of field of view (FOV), spatial resolution, and various forms of imaging artifacts as well as the choice of reconstruction method.

The simplest reconstruction of $M_0(\vec{r})$ can be done by inverse FFT, if the samples are taken at the Cartesian locations in k-space, and the T_2^* relaxation and the phase evolution from ω_0 are ignored. This can be done if a straight line (e.g., in k_x) in k-space is traversed at each RF excitation to keep the signal dephasing and decay time minimal. A 2D imaging example (so called '2D spin-warp') shown in figure 1.1, and an easy extension to 3D imaging (and consequently 3D IFFT for reconstruction) are widely used.

However, these spin-warp type methods are less efficient in terms of scan speed, since after scanning each line, we have to wait for the magnetization to recover its longitudinal component. The recovery of longitudinal component is governed by T_1 recovery time. The T_1 varies in many human tissues, and the typical T_1 of human brain at 3T is between 800 and 1300 ms (table (1.1.1)).

To increase the scan speed, fast single shot methods have been widely used. Two prominent contenders are EPI (Echo Planar Imaging) and spiral trajectories. Unlike

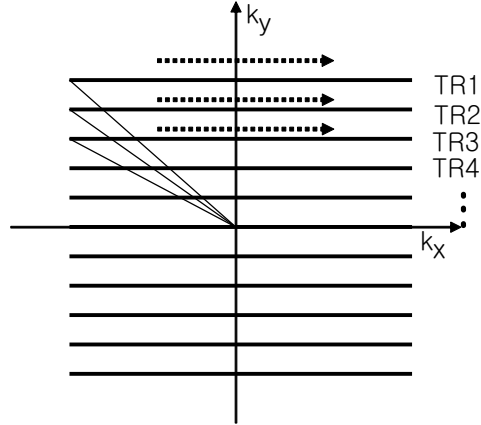


Figure 1.1: Spinwarp acquisition is done by acquiring one line in the 2D k-space after each RF excitation. TR denotes the *repetition time*, which is the time between RF excitations.

spin-warp acquisition, these fast methods use only single excitation, and all the necessary samples to reconstruct M_0 are acquired in a single readout. Therefore, the longer acquisition makes it more susceptible to the effects of ω_0 phase accumulation and T_2^* decay in spin-warp acquisitions.

Figure 1.2 shows the single shot EPI and spiral trajectories. EPI is less efficient in terms of utilizing hardware gradient system, however, it is relatively easier to reconstruct the images via iFFT, and also the artifacts from the field inhomogeneity manifest themselves as pixel shifts. Spiral trajectory is known to be more efficient than EPI, and also robust to flow, but it requires more complicated reconstruction methods since the samples are not on the Cartesian grid points. These two single-shot trajectories are widely used in functional MRI to provide high temporal resolution. The basics of functional imaging are briefly introduced in the next section.

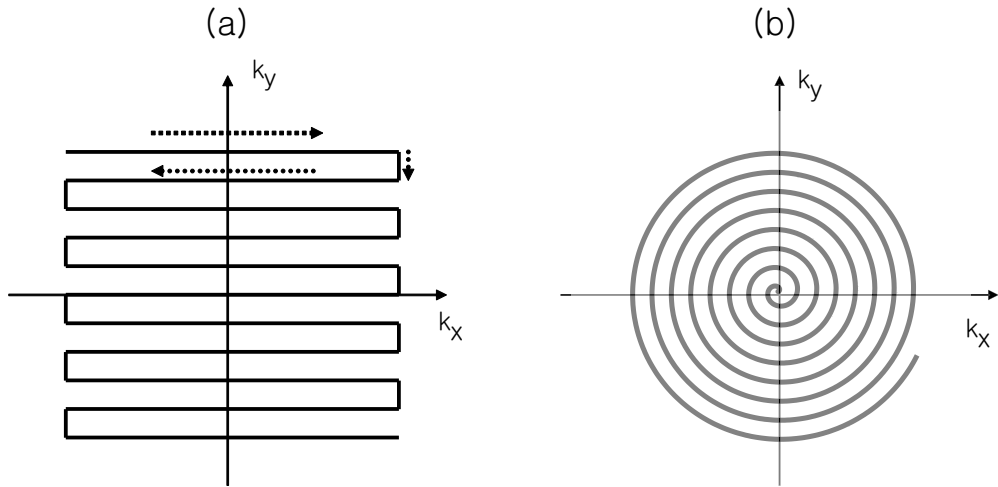


Figure 1.2: (a) Echo Planar Imaging (EPI) trajectory. (b) Spiral trajectory.

1.1.2 Functional magnetic resonance imaging

Functional MRI (fMRI) is an imaging method to explore the function of the human brain, both in normal subjects and in the clinical population. In most fMRI studies, the function of brain is mapped from a set of MR images of a scan subject with a controlled manipulation of a task or stimulus [5–7]. The MR images are directly/indirectly sensitized to the neuronal activities using many contrast mechanisms to provide functional information of human brain. Among the variety of methods, BOLD (Blood Oxygenation Level Dependent) contrast serves as the most widely used method in fMRI community.

BOLD contrast is attributed to the increase of T_2^* near the region of neuronal activation. As the acquisition of the MR images is done at a certain *echo time* repeatedly, the local change of T_2^* can be detected as local increase of image intensity. Even though BOLD effect is an indirect measure of functional activity, which comes

from a complex interact of cerebral blood flow, cerebral blood volume, tissue oxygen extraction and local metabolism, its simplicity and robustness resulted in today's popularity of the method.

A typical BOLD fMRI study is composed of the data collection stage and the data processing stage. In the data collection stage, the gradient echo MR data from the volume of interest are collected repeatedly, while a designed functional task is performed by the scan subject. In the post processing stage, the time series of gradient echo images are reconstructed using appropriate reconstruction algorithm, then statistical analysis is done to determine the activated area dictated by the imposed functional task.

However, the T_2^* weighted BOLD imaging has a couple of disadvantages. Since the method is based on the change of image intensities, it is not easy to compare the results from different subjects or scanners. A more physiologically meaningful comparison can be done by dynamically imaging the T_2^* maps. This can be done by multi-gradient echo sequences [1, 8, 9]. In addition, the dynamic T_2^* mapping provides nearly optimal functional contrast regardless of the spatial distribution of T_2^* in the imaging object, while in T_2^* weighted imaging, the functional contrast is best optimized by acquiring the images at the average T_2^* of the imaging object [8], while individual locations may be still suboptimal.

In chapter III, we introduce the method to estimate dynamic change of R_2^* maps for functional imaging using rosette trajectory.

1.1.3 Rosette trajectory and spectral selectivity

Rosette trajectory

In this section, we bring our focus back to the 2D k-space trajectories used for MR imaging sequences. There are many trajectories that traverse k-space in 2D MRI,

including projection reconstruction (PR), echo-planar, spin-warp, spiral, stochastic, and rosette etc. The rosette trajectory was originally proposed by Likes [10] in 1981 and was reintroduced in spectrally selective imaging techniques [2, 11].

The trajectory is parameterized by two frequency variables, one of which is a rapid oscillation in radial direction (ω_1) and the other is a slow rotation in angular direction (ω_2). Using complex presentation of 2D k-space, we can formulate the trajectory as

$$(1.5) \quad k(t) = k_{max} \sin(\omega_1 t) e^{i\omega_2 t}.$$

Changing ω_1 and ω_2 with k_{max} enables us to control the angular and radial sampling rate of the trajectory in k-space, the size of effective field of view (FOV), spatial resolution. The x and y gradient waveform ($G_x(t)$ and $G_y(t)$) correspond to the time differential of equation (1.5).

In designing a real MR pulse sequence, the hardware requirement should be satisfied. The maximum slew rates and the maximum amplitudes of gradient waveforms are such constraints. The maximum gradient and gradient slew magnitude of a rosette trajectory is given by

$$(1.6) \quad \begin{aligned} |G|_{max} &= \frac{2\pi}{\gamma} k_{max} \omega_1 \\ |S|_{max} &= \frac{2\pi}{\gamma} k_{max} (\omega_1^2 + \omega_2^2). \end{aligned}$$

For example, the maximum gradient amplitude is 4 G/cm, and the maximum gradient slew rate is 180 mT/m/ms in our 3T scanner (EXCITE 2.0, GE medical systems, WI) at the functional MRI laboratory. Figure 1.3 shows examples of rosette trajectories that were designed under these constraints.

Spectral selectivity

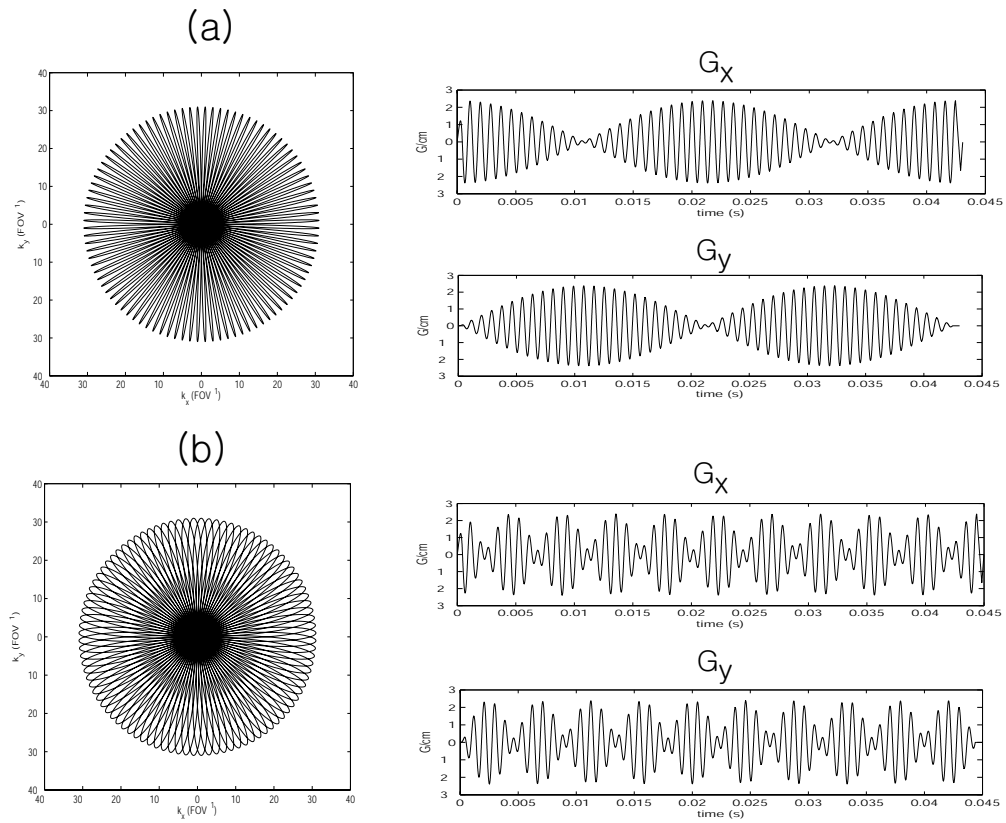


Figure 1.3: (a) A rosette trajectory with $\omega_1=1042$ Hz, $\omega_2=22$ Hz, max slew = 156 mT/m/ms, max gradient = 2.38 G/cm. (b) A rosette trajectory with $\omega_1=1087$ Hz, $\omega_2=113$ Hz, max slew = 171 mT/m/ms, max gradient = 2.38 G/cm.

Since the Larmor relation (1.1) holds at all times, when the magnetic field changes in some area, the resonance frequency of spins in that area also changes. The change of resonance frequency is called *off-resonance frequency*, which is the offset frequency from the main field frequency. The typical source of off-resonance is the susceptibility difference in the imaging object. The abrupt change in the magnetic susceptibility disturbs in the local magnetic field, which leads to immediate perturbation in the resonance frequency near the region. Off-resonance can cause image intensity losses, distortion, and blurring in fast imaging methods such as EPI or spiral.

Likewise, in rosette trajectories, the off-resonance often leads to severe loss of image intensity in the vicinity of large off-resonance. This is due to the frequent visits to the center of k-space during the readout. As the trajectory visits the center of k-space, the extra phase from off-resonance is accumulated, and multiple visits during the long readout causes the vector sum of all DC samples to be canceled out. The degree of loss of image intensity depends on the length of readout and the magnitude of the off-resonance.

Therefore, the off-resonance is considered as another dimension of the imaging, as the self-refocusing trajectories *selectively* reconstructs certain off-resonance frequency (spectral) components (remember that the off-resonance is relative amount with respect to the baseband frequency that we use to demodulate the received signal). The idea of the *spectral selectivity* of rosette trajectory was introduced in [11].

In general, we can define the spectral selectivity of a trajectory as the 2-norm ratio of two images f_0 and $f_{\Delta\omega}$ in ROI,

$$(1.7) \quad P(\omega_{sm}) = \frac{\|f_{\omega_{sm}}\|_2}{\|f_0\|_2}$$

where f_0 is the image reconstructed from unmodulated k-space data ($\omega_{sm} = 0$), and $f_{\omega_{sm}}$ is the reconstructed image from k-space data modulated by $\omega_{sm} \neq 0$. Figure 1.4

shows the spectral selectivity of the trajectories shown in figure 1.3, and reconstructed images with various values of $\omega_{sm}S$.

The FWHM (Full Width Half Maximum) of the main lobe is approximately the reciprocal of the length of rosette acquisition. In multi-shot rosette acquisition, random delays may be added to each shot to reduce the amplitudes of the spectral stopband [11]. Note that the spectral selectivity curves shown in figure 1.4 are imaging object dependent, but the variation between objects will be small.

1.1.4 Spectrally selective imaging

Chemical shift imaging

The idea of spectrally selective imaging is based on the spectral selectivity of rosette trajectory investigated in the previous section. In the original work done by Noll et al. [11], the water and fat components from an imaging object were separated using the difference of the resonance frequencies between two species. This difference is known as chemical shift. At 1.5T, the chemical shift of fat protons is about 220 Hz lower than the resonance frequency of water protons. If the received signal is demodulated at the water proton resonance frequency, the signal from fat protons undergoes extra phase accumulation whenever the rosette trajectory visits the center of k-space during the readout. The image reconstruction from this demodulated data leads to reduction of fat image intensity. In other words, the fat off-resonance is located at the spectral stopband of the spectral selectivity curves shown in figure 1.4, while the water component stays in the spectral passband. Demodulating the received signal at the fat resonance frequency results in the opposite effect, i.e., the fat image retains its image intensity while water image loses most of the image intensity. In summary, a rosette data set is demodulated at the resonance frequencies of water and fat, then water and fat images are reconstructed from each data. This

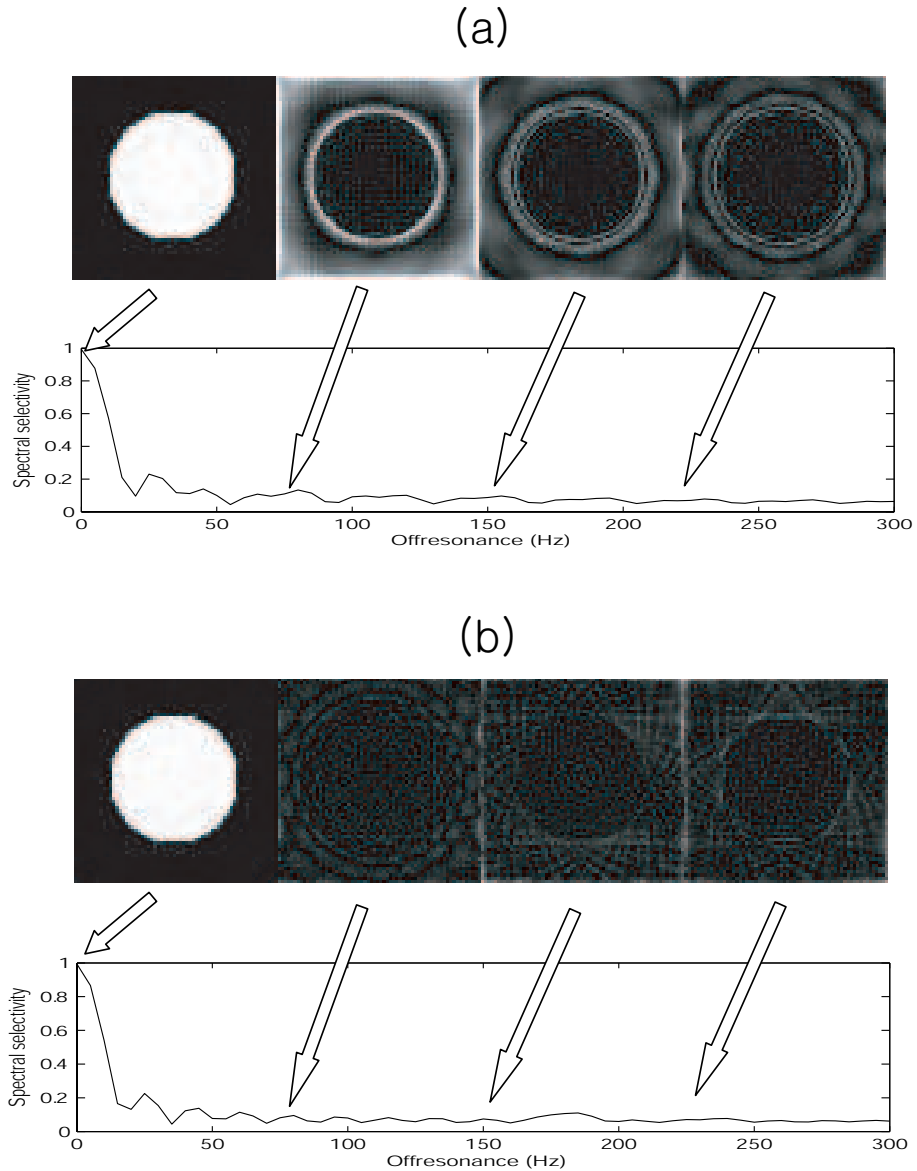


Figure 1.4: (a) Spectral selectivity of the rosette trajectory shown in figure 1.3 (a). This trajectory results in off-resonance artifacts around the edges of the simulation object. The images were reconstructed without off-resonance correction, where the k-space data was modulated by the off-resonance frequencies (0 Hz, 75 Hz, 150 Hz, 225 Hz) indicated by the arrows. (b) Spectral selectivity of the rosette trajectory shown in figure 1.3 (b). Unlike the previous example, this trajectory has very good suppression of the simulation object at nonzero off-resonance locations.

method is advantageous over other chemical shift imaging methods based on Dixon's method [12, 13], since it requires only one data acquisition.

Since the data samples in k-space do not lie on the Cartesian grid, the field-map corrected reconstruction was done using the convolution gridding method [14, 15] combined with time-segmented field correction technique [16].

SMART(Simultaneous Multislice Acquisition using Rosette Trajectories) imaging

The principle of spectrally selective imaging was extended to a fast multi-slice imaging technique called SMART [2]. In this method, three slices are excited at one time, and a constant gradient in slice-select direction, G_{sm} , is applied during the readout to induce distinct off-resonance frequencies within each of those slices. Figure 1.5 shows the gradient wave forms and RF pulse used in this method. In this method, the slices are equally spaced, so the resonance frequency difference between adjacent slices are equal. We define the resonance frequency difference between slices as $\omega_{sm} \triangleq \gamma G_{sm} z_0$, where z_0 is the center-to-center slice distance. Similar to the chemical shift imaging, ω_{sm} works as an artificial *chemical shift* frequency, and the spectral selectivity of rosette trajectory allows separation of three spectral components, that, in this case, are the three simultaneously excited slices.

In [2], each image is reconstructed from demodulated SMART data sets using field-map corrected convolution gridding method. Figure 1.6 shows three slices of a human brain reconstructed from the SMART acquisition, as well as the conventional single slice image at one of the identical locations. As it was pointed out by Noll et al., SMART images have lower approximate SNR due to the artifacts from the off-resonant slices. The functional imaging result (activation map in the third column) shows that the activation areas of SMART images are very similar to that of the

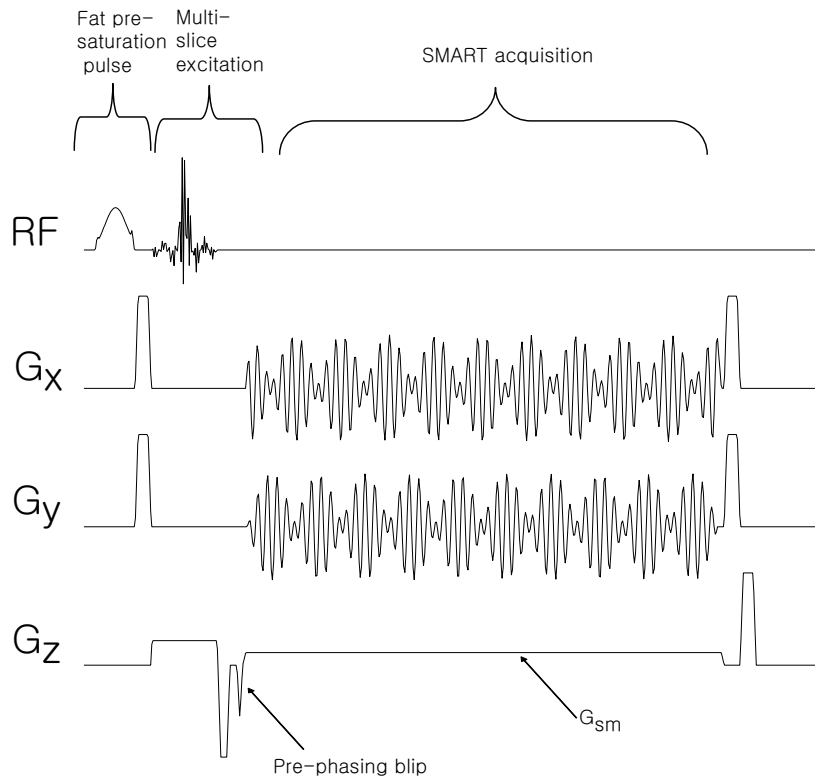


Figure 1.5: Pulse sequence for SMART imaging. The pulse sequence is very similar to the conventional single shot gradient echo imaging sequence except for the SMART gradient and the multi-slice excitation RF pulse.

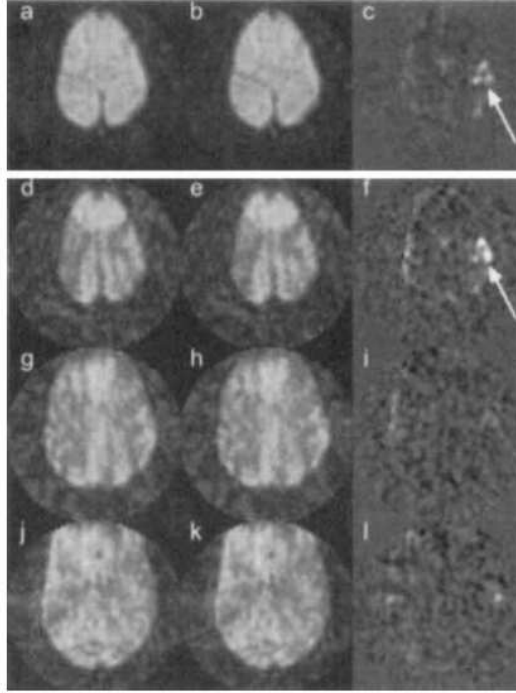


Figure 1.6: Figure 5 of [2]. "Comparison of single-slice rosette acquisition (a-c) and triple-slice SMART acquisition (d-l) for experimental data acquired using the single-shot rosette trajectory. Images are presented for the average control condition (a,d,g,j), the average active condition (b,e,h,k), and the average difference (x 60) of active and control conditions (c,f,i,l). Activation areas are marked with arrows" [2]. Note that this experiment was performed using 1.5 T scanner, and the in-plane spatial resolution was kept to 5 mm to accommodate the hardware limitations (max slew rate 120 mT/m/ms).

single slice image. The received signal of SMART acquisition, which is demodulated at the resonance frequency of the middle slice, can be written as

$$(1.8) \quad S_{\text{SMART}}(t) = S_{\text{slice}_1}(t) + S_{\text{slice}_2}(t) + S_{\text{slice}_3}(t) + \epsilon(t)$$

where

$$\begin{aligned}
S_{slice_1}(t) &= \int_{-\frac{\Delta z}{2}+z_0}^{\frac{\Delta z}{2}+z_0} e^{-i\gamma(G_{sm}t+\phi_0)z} dz \iint M_1(x, y) e^{-i2\pi(k_x(t)x+k_y(t)y)} e^{-i\omega_1(x,y)t} dx dy \\
&= E_z(t) \cdot e^{-i\gamma(G_{sm}t+\phi_0)z_0} \iint M_1(x, y) e^{-i2\pi(k_x(t)x+k_y(t)y)} e^{-i\omega_1(x,y)t} dx dy, \\
S_{slice_2}(t) &= \int_{-\frac{\Delta z}{2}}^{\frac{\Delta z}{2}} e^{-i\gamma(G_{sm}t+\phi_0)z} dz \iint M_2(x, y) e^{-i2\pi(k_x(t)x+k_y(t)y)} e^{-i\omega_2(x,y)t} dx dy \\
&= E_z(t) \iint M_2(x, y) e^{-i2\pi(k_x(t)x+k_y(t)y)} e^{-i\omega_2(x,y)t} dx dy, \\
S_{slice_3}(t) &= \int_{-\frac{\Delta z}{2}-z_0}^{\frac{\Delta z}{2}-z_0} e^{-i\gamma(G_{sm}t+\phi_0)z} dz \iint M_3(x, y) e^{-i2\pi(k_x(t)x+k_y(t)y)} e^{-i\omega_3(x,y)t} dx dy \\
&= E_z(t) \cdot e^{i\gamma(G_{sm}t+\phi_0)z_0} \iint M_3(x, y) e^{-i2\pi(k_x(t)x+k_y(t)y)} e^{-i\omega_3(x,y)t} dx dy, \\
E_z(t) &= \frac{2 \sin(\gamma(G_{sm}t + \phi_0) \frac{\Delta z}{2})}{\gamma(G_{sm}t + \phi_0)}, \\
\phi_0 &= -G_{sm}T_{acq}/2.
\end{aligned}$$

z_0 denotes the center-to-center slice distance; Δz is the slice thickness; $\omega_1, \omega_2, \omega_3$ are susceptibility induced off-resonance of each slice; ϕ_0 is the gradient-time area of the prephasing gradient blip; T_{acq} is the length of the readout; and $\varepsilon(t)$ is the complex Gaussian noise.

The magnitude of G_{sm} needs to be big enough to be able to give enough suppression of the off-resonant slices ($slice_1$ and $slice_3$ in equation (1.8)). At the same time, it should be small enough to ensure that the spectral stopbands do not clip off the outer part of the slices, and the through-slice dephasing term, $E_z(t)$, should not have any zeros during the data acquisition. These constraints are summarized as

$$(1.9) \quad \frac{2\pi}{\gamma z_0 T_{acq}} < G_{sm} < \frac{2\pi}{\gamma \Delta z T_{acq}}.$$

Therefore, depending on the total number of slices to be imaged, the slice distance and slice thickness should be determined, and the magnitude of G_{sm} should be determined using equation (1.9).

In addition, if there is significant susceptibility induced off-resonance in each slice, ω_{sm} should be bigger than the maximum of off-resonance in each slice. Equation 1.9 then should be modified to

$$(1.10) \quad \frac{4\pi\omega_{max}}{\gamma z_0} < G_{sm} < \frac{2\pi}{\gamma\Delta z T_{acq}}$$

where ω_{max} is the maximum absolute value among ω_1, ω_2 , and ω_3 .

1.1.5 Image Reconstruction for non-Cartesian sampling in MRI

In this section, we briefly overview two field-map corrected reconstruction methods called conjugate phase reconstruction method [16–18], and physics model based iterative reconstruction method [19]. The rest of the section covers convolution gridding [20] and NUFFT (NonUniform Fast Fourier Transform) [21] as methods to accelerate those field-map corrected reconstruction methods. In chapters II and III, NUFFT serves an essential building block of the proposed reconstruction methods.

CP (Conjugate Phase) reconstruction

The conjugate phase reconstruction is based on the simple idea to *rewind* all the phase accumulation due to off-resonance [16–18]. Using the notations of equation (1.1.1), the field-map corrected image reconstructed using conjugate phase is

$$(1.11) \quad \hat{x}(\vec{r}_n) = \sum_{m=1}^M W_m S_r(t_m) e^{i\omega_0(\vec{r}_n)} e^{i2\pi\vec{k}_m \cdot \vec{r}}$$

where W_m is a density weight compensation function sampled at k-space sampling locations. To avoid direct evaluation of conjugate phase, which is computationally expensive, time-segmented and frequency segmented approximations were proposed [16, 18]. In time-segmented approximation, the received data is time-segmented, and each segment is reconstructed using a fast convolution gridding method, then the images are combined linearly to form the field-map corrected image.

In frequency-segmented approach, a similar procedure is done, in multiple segments in the off-resonance frequency domain. Although, these methods can correct for the off-resonance artifacts, its success heavily depends on the assumption of smooth field map. The physics model based iterative reconstruction does not require such assumption, and works better in the brain regions where the field map has high spatial gradient.

Physics model based iterative reconstruction

From the MR signal equation (1.4), we can establish a discrete matrix-vector formulation.

The object can be represented as sum of basis functions $b_j(x, y, z)$ and its coefficients $c_j(x, y, z)$ [19]

$$(1.12) \quad M_0(x, y, z) = \sum_j c_j(x, y, z) \cdot b_j(x, y, z).$$

The simplest choice of b_j and c_j will be Dirac impulses $\delta(x)\delta(y)\delta(z)$ and the M_0 evaluated at Cartesian grid points (x_i, y_i, z_i) , i.e.

$$(1.13) \quad M_0(x, y, z) = \sum_{i=1}^N M_0(x_i, y_i, z_i) \delta(x - x_i) \delta(y - y_i) \delta(z - z_i).$$

Substituting equation (1.13) into equation (1.4) results in the discrete formulation of the MR signal equation, and $X = M_0(x_i, y_i, z_i)$ becomes the object to be reconstructed from the formulation, i.e., given M samples of the received signal $Y \in \mathbb{C}^M$,

$$(1.14) \quad Y = AX + n,$$

where

$$[A]_{ji} = e^{-i2\pi(k_x(t_j)x_i + k_y(t_j)y_i)} e^{-i\omega(x_i, y_i)t_j}, \quad i = 1, \dots, N, \quad j = 1, \dots, M,$$

$X \in \mathbb{C}^N$ is the object, $\omega(x, y)$ is off-resonance from field inhomogeneity, and $n \in \mathbb{C}^M$ is bi-variate white Gaussian noise. The primary source of the noise in MR system is

considered to be the electrical random fluctuation caused by the Brownian motion of electrons in the receiver coil and the body [4]. This noise is added to the raw received signal and goes through the quadrature detection-demodulation to result in an additive complex white Gaussian noise.

The reconstruction of X can be done by Maximum Likelihood Estimation (MLE), and the estimator is given as the least square form,

$$\begin{aligned} \hat{X}_{MLE} &= \underset{X}{\operatorname{argmin}} \|Y - AX\|^2 \\ (1.15) \quad &= [A^*A]^{-1}A^*Y. \end{aligned}$$

However, the matrix inversion, in general, is an ill-conditioned problem. Even if the inverse exists at all, it requires a regularization term added to the (1.15). The quadratic function is one of the simplest forms of regularization, but easier to analyze. This penalizes the roughness of neighboring pixels,

$$\begin{aligned} R(X) &= \sum_{i=2}^N (X_i - X_{\text{previous in horizontal direction}})^2 \\ &\quad + \sum_{i=2}^N (X_i - X_{\text{previous in vertical direction}})^2 \\ (1.16) \quad &= \|CX\|^2, \end{aligned}$$

where $C = \begin{bmatrix} C_1 \\ C_2 \end{bmatrix} \in R^{2(N-1) \times N}$, and

$$C_1 = \begin{bmatrix} -1 & 1 & 0 & \cdots & 0 \\ 0 & -1 & 1 & \cdots & 0 \\ & & \ddots & \ddots & \\ 0 & \cdots & 0 & -1 & 1 \\ 1 & 0 & \cdots & 0 & -1 \end{bmatrix}, \quad C_2 = \begin{bmatrix} -1 & 0 & \cdots & 0 & 1 & 0 & \cdots & 0 \\ 0 & -1 & \cdots & 0 & 0 & 1 & \cdots & 0 \\ & & \ddots & & & & \ddots & \\ 0 & 0 & -1 & 0 & \cdots & 0 & 1 & 0 \\ 0 & 0 & \cdots & -1 & 0 & \cdots & 0 & 1 \end{bmatrix}.$$

Adding the equation (1.15) to the cost function in equation (1.16) yields the Quadratic Penalized Least Square (QPLS) cost function. The physics model based iterative reconstruction is finding the minimizer of the cost function

$$\begin{aligned}
 \hat{X}_{MLE} &= \underset{X}{\operatorname{argmin}} \|Y - AX\|^2 + \beta \|CX\|^2 \\
 (1.17) \qquad &= [A^*A + \beta C^*C]^{-1} A^*Y.
 \end{aligned}$$

Because the inversion of the MR system matrix (A^*A) is such a large scaled problem, and can be also numerically unstable, an iterative approach is desirable which is numerically stable, convergent, and fast. Among the many iterative methods, the Conjugate Gradient (CG) [22] is used. When the matrix to be inverted is hermitian and positive definite, the algorithm achieves zero norm of the error at finite number of iteration, under the assumption of no numerical noise. If the matrix is well behaved either by itself or by pre-conditioning, the method achieves a desired accuracy much earlier than the maximum number of iterations [23].

The regularization parameter β can be chosen as the maximum value that gives the maximum resolution for the grid size. This was done by observing the point spread function (PSF) of the estimator. A fast calculation of local PSF based on FFT [24] is often used for quick determination of β .

Convolution gridding and NUFFT (NonUniform Fast Fourier Transform)

In CP reconstruction and physics-based iterative reconstruction, the most computationally intensive part boils down to the calculation of the image pixel values at Cartesian grid points from non-Cartesian Fourier data, and vice versa. In this thesis, we call the estimation of image pixel points from k-space reconstruction as *MR inverse problem*, and the calculation of non-Cartesian k-space samples as *MR*

forward problem.

The most popular way to accelerate the MR forward/inverse problems is to use 2D FFT with 2D interpolation. For MR inverse problem, a method known as *convolution gridding* [20] has been used in many MR applications as a fast non-iterative way of reconstructing images for non-Cartesian k-space trajectories. The convolution gridding procedure is described as

$$(1.18) \quad \hat{X} = IFFT[(Y \cdot W) \otimes C]/c$$

where the sampled MR data Y is multiplied by the density compensation function (DCF) W , convolved with a chosen 2D convolution function C , the inverse FFT is applied, and divided by the inverse Fourier transform of the convolution kernel.

The finite support convolution function C gives a way to a practical implementation of the algorithm compared to the optimal sinc interpolator. In [14], the Kaiser-Bessel function is found to be the best choice, since it is simple to calculate for the price of slight sacrifice in the interpolation performance. However, this function (and other possible choices of convolution functions) often results in rolloff at the edge of the FOV. Therefore, the division of c is necessary to make the response to be flat in the FOV. Since the division by c also makes the sidelobes of the response function to be amplified, it is often recommended to grid the non-Cartesian data to oversampled grid points to increase the effective FOV [20]. The DCF (W) makes a correction for a nonuniform sampling density of the non-Cartesian trajectory. The DCF can be calculated directly from the analytical expression of k-space trajectory [25,26], or from local sampling density of the trajectory [27,28]. An alternative method was also suggested by Pipe [29] that iteratively calculated DCF from a necessary condition for correct reconstruction in an ROI (Region Of Interest). Apart from the original formulation by O'Sullivan, Rosenfeld [30] suggested a least square solution to grid-

ding, and Sedarat [31] showed that both formulation can be expressed in similar linear equation and calculated the least square approximation of DCF to Rosenfeld's formulation.

The MR forward problem requires a similar approach to convolution gridding. In fact, it corresponds to the *problem 2* of NUFFT using the nomenclature of [21]. The problem 2 is defined as a fast calculation of the following expression

$$(1.19) \quad X(\omega_m) = \sum_{n=0}^{N-1} x_n e^{-i\omega_m n}, \quad m = 1, \dots, M$$

where $X(\omega_m)$ is FT of x evaluated at the non-Cartesian frequency locations ω_m , and x_n are the given samples at the Cartesian grid locations. In NUFFT literature, there are many ways to evaluate equation 1.1.5 including [21, 32–34], where each method differ by the choice of the interpolation kernels. In this section, we briefly overview the derivation of [32], which is used in the developed methods in chapters II and III.

The NUFFT is described by the following equation

$$(1.20) \quad \hat{X}(\omega_m) = \sum_{k=0}^{K-1} v_{mk}^* \sum_{n=0}^{N-1} x_n e^{-i2\pi k/Kn}, \quad m = 1, \dots, M,$$

in other words, a weighted K -point ($K \geq N$) FFT is done on the Cartesian samples x_n , then appropriate interpolation using neighboring samples is done to quickly determine the non-Cartesian Fourier coefficients at ω_m . The *scaling factor* was first introduced in [33], and it serves as precompensation for the imperfections in the subsequent frequency-domain interpolation. Note that the adjoint operator combined with DCF precompensation is an equivalent method to the convolution gridding.

In [32], the min-max interpolation coefficients were found by solving a simple least square problem. The min-max interpolator was also shown to give the best interpolation accuracy among other conventional interpolation kernels. But, once again, Kaiser Bessel function was found to have very close interpolation accuracy

to the min-max interpolator. Therefore, in our works, we used the Kaiser-Bessel interpolator in the NUFFT implementation.

Using the combination of NUFFT and the time-segmented approximation for off-resonance as well as the adjoint operation, a fast CG iteration for iterative MR image reconstruction is done [19].

CHAPTER II

Iterative Reconstruction for SMART Imaging

2.1 Introduction

Fast dynamic 3D imaging methods can benefit numerous MR applications including diffusion imaging, perfusion imaging, functional imaging, cardiac imaging, and real-time imaging. Increased imaging speed can result in increased temporal/spatial resolution, or increased signal to noise ratio via averaging of the signal. One way of accelerated imaging would be increasing gradient switching rate and gradient amplitude, which allow faster sampling in k-space. However, there is a limitation to this approach as high temporal variation of gradient can cause discomfort of a subject due to the peripheral nerve stimulation [35].

Another approach is sparse sampling in k-space and filling up the missing data points via appropriate interpolation with a priori information on the imaging object or data samples acquired in other time points. Such methods include keyhole imaging [36,37], generalized series reconstruction (RIGR) [38], k-t BLAST [39] and UNFOLD [40].

The recent development of parallel imaging techniques [41,42] also enabled significant acceleration of MR acquisition, where the extra information of coil sensitivity maps or a low resolution calibration scans help the reconstruction algorithms to

determine the missing data samples.

SMART imaging was introduced by Noll et al. [2] as another yet unique method for fast 3D volume imaging. Rather than using interpolations for missing data or extra equipment such as array coils, it used the intrinsic property of the sampling pattern of rosette trajectories. The rosette trajectory has been known for its spectral selectivity due to the repeated sampling of the origin of k-space during the readout [11]. In SMART, three slices are excited followed by a constant gradient in the slice select direction during the readout, which imposes distinctive off-resonance to each slice. Each slice is then reconstructed using conjugate phase reconstruction [17] after demodulating the k-space data by the corresponding off-resonances. Noll et al. successfully demonstrated that this method provides nearly equivalent functional detectability compared to the conventional single slice imaging. However, this work was demonstrated only in a 1.5T scanner, and the conjugate phase reconstruction of each slice led to significant off-resonance artifacts in the reconstructed images.

According to the basic MR physics, increasing the main magnetic field is desirable since it increases the MR signal strength. Therefore, implementing SMART in 3T would be beneficial for a higher detectability of functional studies. However, in 3T systems, the conjugate phase reconstruction can be an unfavorable choice, since the MR physics dictates that the susceptibility induced off-resonance doubles at 3T compared to 1.5T. The increased off-resonance causes more artifact especially in the brain areas near ear canals and sinus, and the conjugate phase reconstruction often fails to recover image intensity at the locations with high spatial gradient of the off-resonance [19]. Among many other field-map corrected image reconstruction methods, physics model-based iterative reconstruction via minimization of the quadratic penalized cost function [19] recovers the image intensity in areas with high

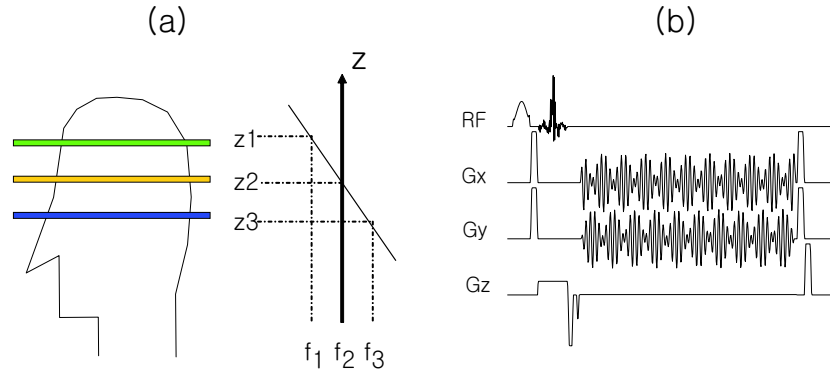


Figure 2.1: (a) Diagram of SMART method. Three slices at locations z_1 , z_2 , and z_3 are excited simultaneously. During the readout, a linear gradient in slice-select direction is played to introduce spatially constant off-resonance at each slice location. (b) Pulse sequence of SMART acquisition

spatial gradient of off-resonance, while allowing flexible modification of the system model.

In this chapter, we extend the physics model based iterative reconstruction to the image reconstruction of SMART method. The proposed iterative SMART reconstruction (iSMART) recovers image intensity at the areas with higher susceptibility-induced off-resonance in 3T, and also reduces much of the static off-resonance artifacts. Simulation results are shown to demonstrate the improved accuracy in the image reconstruction compared to the conventional conjugate phase SMART reconstruction. A functional study result is also shown to demonstrate the effectiveness of the proposed method.

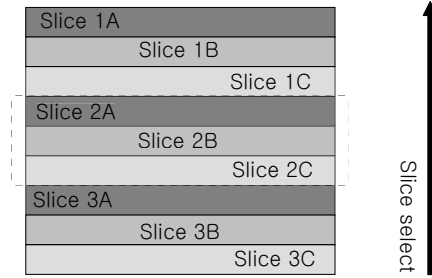


Figure 2.2: An example of a SMART acquisition to cover a 3D volume. Slices 1A,2A,3A are simultaneously excited, and the excitation of slices 1B,2B,3B and 1C,2C,3C follow. In order to fill up the space without a gap, the center-to-center slice distance should be one third of the thickness of the 3D volume. Only the slices in the dashed box need to be prescribed in the scanner.

2.2 Theory

2.2.1 SMART acquisition

Figure 2.1 (a) depicts the SMART acquisition method. In this method, three different slices are excited simultaneously using the linear sum of sinc pulses modulated by off resonance frequencies, and the constant gradient in slice-select direction (G_{sm}) is applied during the readout as shown in the pulse sequence diagram (figure 2.1). Figure 2.1 reveals that the pulse sequence for SMART acquisition differs from the conventional gradient echo sequences only by the multi-slice excitation pulse in RF channel, and G_{sm} . G_{sm} is preceded by the refocusing gradient, since G_{sm} results in additional sinc modulation to the received signal due to the through-plane dephasing. The prephasing gradient blip brings the peak of the sinc envelope to the middle of the acquisition in order to avoid having zeros of the sinc envelope during the acquisition. Therefore, there is slight increase of scan time ($\approx 200\mu s$) compared to the conventional single-slice gradient echo rosette imaging.

In multi-slice imaging, the SMART data is acquired at multiple locations to cover a 3D volume. To cover a 3D volume without a gap, we need to set the center-to-center distance between simultaneously excited slices as one third of the thickness of the entire volume. Figure 2.2 illustrates how the slice selections are done for a 3D volume coverage.

2.2.2 SMART system model

We can easily calculate the off-resonance frequency of each slice location from the slice thickness, slice distance and the magnitude of G_{sm} , for the isocenter of the slice select gradient is set to the center of the prescribed volume in the MR scanner. After demodulating each data to the resonance frequency of the middle slice, the baseband signal of SMART acquisition is the sum of signals from the simultaneously excited slices as

$$(2.1) \quad S_{\text{SMART}}(t) = S_{\text{slice}_1}(t) + S_{\text{slice}_2}(t) + S_{\text{slice}_3}(t) + \epsilon(t)$$

where

$$\begin{aligned} S_{\text{slice}_1}(t) &= \int_{-\frac{\Delta z}{2}+z_0}^{\frac{\Delta z}{2}+z_0} e^{-i\gamma(G_{sm}t+\phi_0)z} dz \iint M_1(x, y) e^{-i2\pi(k_x(t)x+k_y(t)y)} e^{-i\omega_1(x,y)t} dx dy \\ &= E_z(t) \cdot e^{-i\gamma(G_{sm}t+\phi_0)z_0} \iint M_1(x, y) e^{-i2\pi(k_x(t)x+k_y(t)y)} e^{-i\omega_1(x,y)t} dx dy, \\ S_{\text{slice}_2}(t) &= \int_{-\frac{\Delta z}{2}}^{\frac{\Delta z}{2}} e^{-i\gamma(G_{sm}t+\phi_0)z} dz \iint M_2(x, y) e^{-i2\pi(k_x(t)x+k_y(t)y)} e^{-i\omega_2(x,y)t} dx dy \\ &= E_z(t) \iint M_2(x, y) e^{-i2\pi(k_x(t)x+k_y(t)y)} e^{-i\omega_2(x,y)t} dx dy, \\ S_{\text{slice}_3}(t) &= \int_{-\frac{\Delta z}{2}-z_0}^{\frac{\Delta z}{2}-z_0} e^{-i\gamma(G_{sm}t+\phi_0)z} dz \iint M_3(x, y) e^{-i2\pi(k_x(t)x+k_y(t)y)} e^{-i\omega_3(x,y)t} dx dy \\ &= E_z(t) \cdot e^{i\gamma(G_{sm}t+\phi_0)z_0} \iint M_3(x, y) e^{-i2\pi(k_x(t)x+k_y(t)y)} e^{-i\omega_3(x,y)t} dx dy, \\ E_z(t) &= \frac{2 \sin(\gamma(G_{sm}t + \phi_0) \frac{\Delta z}{2})}{\gamma(G_{sm}t + \phi_0)}, \\ \phi_0 &= -G_{sm}T_{acq}/2. \end{aligned}$$

In the equation 2.1, z_0 denotes the slice distance; Δz is the slice thickness; $\omega_1, \omega_2, \omega_3$ are susceptibility induced off-resonance of each slice; ϕ_0 is the gradient-time area of the prephasing gradient blip; T_{acq} is the length of the readout; and $\varepsilon(t)$ is the complex Gaussian noise added to the received signal. In addition, we define the resonance frequency difference between slices as $\omega_{sm} \triangleq \gamma G_{sm} z_0$.

The through-plane dephasing term $E_z(t)$ is expressed as a sinc function only when the excitation slice profile is a perfect rect. In real experiments, this function may deviate from a sinc function due to the imperfect slice profile. In general, $E_z(t)$ is a Fourier transform of the excitation profile. In addition, the spatial gradient of the susceptibility-induced off-resonance within a voxel also can contribute to the through-plane dephasing, which is spatially varying. Since the spatial gradient can be easily calculated from a measured 3D field map, this term can be included as the extra dephasing in the signal equation. In this work, we assume the effect of spatial gradient of field map is negligible.

Considering the intra voxel dephasing on the imaging plane [19], the transverse magnetization is expressed as sum of rect basis functions

$$(2.2) \quad M_k(x, y) = \sum_{i=1}^N M_k(x_i, y_i) \Pi(x - x_i) \Pi(y - y_i), \quad k = 1, \dots, 3.$$

Substituting equation (2.2.2) into (2.1) and sampling in time results in the discretized linear SMART signal equation:

$$(2.3) \quad Y = AX + \varepsilon$$

where

$$\begin{aligned}
A &= [D(E_z(t_j)E_1(t_j)) A_1 \quad D(E_z(t_j)) A_2 \quad D(E_z(t_j)E_3(t_j)) A_3], \\
X &= \begin{pmatrix} X_1 \\ X_2 \\ X_3 \end{pmatrix}, \\
E_1(t_j) &= e^{-i\omega_{sm}t_j}, \\
E_3(t_j) &= e^{i\omega_{sm}t_j}, \\
[A_k]_{ji} &= \Phi(t_j)e^{-i2\pi(k_x(t_j)x_i+k_y(t_j)y_i)}e^{-i\omega_k(x_i,y_i)t_j}, \\
i &= 1, \dots, N, \quad j = 1, \dots, M, \quad k = 1, 2, 3,
\end{aligned}$$

$D(\cdot)$ denotes a diagonal matrix, X_1, X_2, X_3 are the vectors which are the lexicographically rearranged samples of slices 1,2,3 at locations (x_i, y_i) , and ε denotes a noise vector. Note that the constant phase terms $e^{\pm i\gamma\phi_0z_0}$ in equation (2.1) for slices 1 and 3 were not included in the equation (2.3), therefore the reconstructed images of those slices will have extra constant phase from the refocusing SMART gradient. In the SMART system model, the discrete locations (x_i, y_i) are limited to a circular support that covers typical brain images in the FOV to reduce the number of unknowns, or the length of the vector X . For the rosette trajectory we used in this work, the number of unknowns was smaller than the number of samples. Therefore, the system model remains over-determined as in the conventional single slice reconstruction problems.

2.2.3 Conjugate phase and single slice iterative reconstructions for SMART

As was described in the section 1.1, the conjugate phase reconstruction for SMART data was proposed by Noll et al. in their original paper [2]. The recon-

struction is done by demodulating the SMART data to the resonance frequencies of each slice, then applying conjugate phase reconstruction to each demodulated data. In this work, we call this method simply as CPSMART method.

One could think of another yet similar reconstruction method, since conjugate phase reconstruction is not known to be the best choice when field map has high spatial gradient [19]. In lower brain areas, the physics model-based iterative reconstruction proposed by Sutton et al. [19] was reported to be superior compared to the conjugate phase reconstruction. Therefore, it is a natural extension to use the iterative reconstruction to each demodulated SMART data set for a better correction for the off-resonance. We refer this method as single slice iterative reconstruction for SMART, or ssiSMART.

2.2.4 Iterative SMART reconstruction (iSMART)

The reconstruction of the discrete images X_1, X_2, X_3 can be done by solving the inverse problem of the equation (2.3). Extending the single slice case discussed in section 1.1 to SMART system equation, the ML estimator of the object from the observed data Y with quadratic roughness penalty is

$$\begin{aligned}
 \hat{X}_{MLE} &= \underset{X}{\operatorname{argmin}} \|Y - AX\|^2 + \beta \|C_{SM}X\|^2 \\
 (2.4) \qquad &= [A^*A + \beta C_{SM}^*C_{SM}]^{-1} A^*Y
 \end{aligned}$$

where

$$(2.5) \qquad C_{SM} = \begin{pmatrix} C & 0 & 0 \\ 0 & C & 0 \\ 0 & 0 & C \end{pmatrix},$$

and C is the finite difference matrix as defined in section 1.1. The minimization of the cost function is done by applying conjugate gradient algorithm. For each iteration,

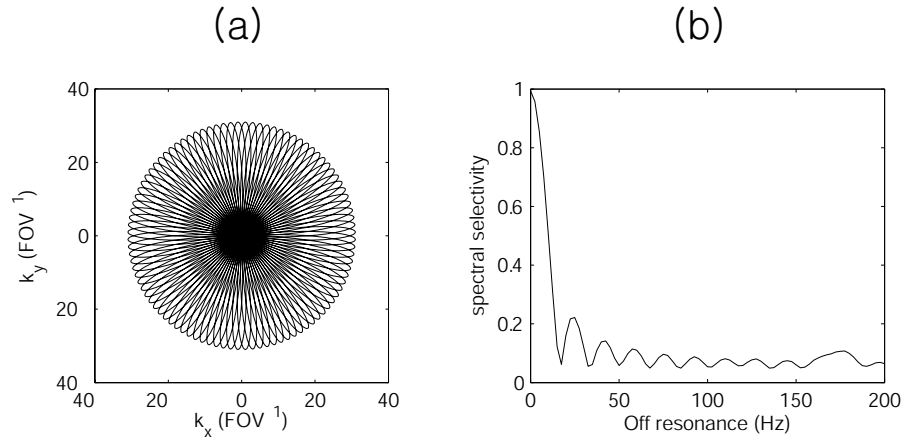


Figure 2.3: (a) Rosette trajectory. (b) Spectral selectivity of the rosette trajectory in (a).

the most time consuming matrix-vector multiplications were accelerated by using the combination of time-segmented approximation with min-max interpolator and NUFFT [19].

In the SMART system model, there are many components that affect the quality of the reconstruction. The susceptibility-induced off-resonance maps, i.e. $\omega_1, \omega_2, \omega_3$ have to be measured in separate scans, and the through-slice dephasing term E_z also have to be measured due to the unideal gradient characteristics and the excitation profiles.

In the following section, we describe how to measure the data and such components for the accurate reconstruction of the SMART images as well as the simulation studies to demonstrate and compare the effect of those components on the CPSMART, ssiSMART, and iSMART reconstruction methods.

2.3 Methods

Figure 2.3 shows the rosette trajectory and its spectral selectivity used in the simulations and scan experiments. First, the number of petals were decided to be 96, which led to 192 angular sampling, where the number of angular sampling to ensure

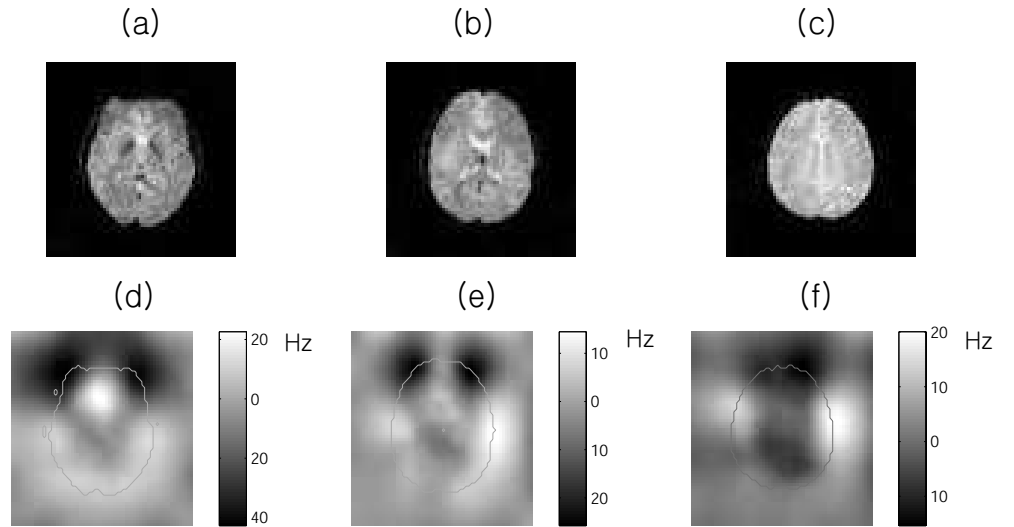


Figure 2.4: (a)-(c) The reference images used in the simulation. (d)-(f) The reference field maps used in the simulation overlaid with the support of the reference images.

Nyquist sampling at the edge of the k-space was 201. Since the ratio between the fast oscillation frequency (radial direction) and the slow oscillation frequency (angular direction) decides the location of the secondary peak in the spectral selectivity, the ratio was carefully chosen not to have the secondary peak at ω_{sm} . The fast frequency was 1041.7 Hz, and the slow frequency was 108.5 Hz. The sampling time was 4 μ s, and the total readout was 46.3 ms. The SMART off-resonance ω_{sm} was 165 Hz.

2.3.1 Simulation study

Figure 2.4 shows the reference discrete objects and the corresponding field maps. The supports overlaid on the field map (figure 2.4 (d)-(f)) indicate the regions inside the objects. The supports were used when the normalized root mean squared error was measured with respect to the reference images. On the other hand, three identical circular supports (radius 28 voxels) were used in the reconstruction to reduce the number of pixels to be reconstructed.

Comparison of reconstruction methods

Using the reference images and the field maps, a SMART data set was synthesized using equation (2.3). In the system model, we used the through slice dephasing term E_z , which was measured in another scanner experiment. A complex Gaussian random noise was added to the data set, and the variance of noise was set to 40dB (100 to 1) SNR.

Using the reference field maps, field-map corrected reconstructions were done using CPSMART, ssiSMART, and iSMART. For ssiSMART reconstruction, the spatial regularization parameter was set to 1. The spatial regularization parameter was determined as the value that resulted 1.28 pixels of the FWHM of the point spread function of the reconstruction. Similarly, the spatial regularization parameter was set to be 10 for iSMART reconstruction. At each iteration, NRMSE was measured with respect to the reference images inside the objects for each slice. NRMSE was also measured for the CPSMART reconstructions in a similar way.

Sensitivity to the field map error

The second set of simulations were done to investigate the sensitivity of each reconstruction methods to the error of the field maps used in the field-map corrected reconstruction. As in the first simulations, a SMART data set was synthesized using equation (2.3) with 40 dB SNR and the reference images and the field maps shown in figure 2.4. For each reconstruction method, field-map corrected reconstructions were performed using field maps that are scaled by factors $1.0 \sim 2.0$. The scale factors introduced spatially non uniform errors in the field maps used in the reconstruction up to 18 Hz root mean square error. The NRMSE was measured with respect to the reference images in the object for each reconstruction method.

Spatial resolution comparison

To investigate the spatial resolution of each reconstruction method, two SMART data sets were synthesized and reconstructed using each reconstruction method. One data set was synthesized using the reference images in figure 2.4, and the other data set was synthesized using a perturbed image, which is sum of the reference image and a dirac delta function located in the middle of FOV. The perturbation was done to the slice 2. The point spread function was determined by subtracting the magnitude images of all slices reconstructed from perturbed/unperturbed SMART data, and the full width half maximum of the point spread function was measured.

In the spatial resolution simulation, field maps were not used in the system model, since they can introduce extra spatial non uniformity in the point spread function of the reconstruction. The simulated data was noiseless, as noisy data makes it hard to estimate the full width half maximum when the amplitude of the point spread function is low compared to the noise strength.

2.3.2 Experimental study

For a series of system parameter measurements and functional experiments, a scan subject was recruited, and provided with the informed consent in accordance with the guideline of the University of Michigan institutional review board. All scan experiments were performed using a 3T scanner (EXCITE 2.0, GE medical systems, Waukesha, WI).

Measurement of field map

A vendor-provided high order shimming was performed prior to the scan experiment. The initial field maps were estimated using 8 shot rosette gradient echo images with single slice excitations. Two different echo times ($TE_1=27.5$ ms, $TE_2=30$ ms) were used to estimate the field maps of each slice from the phase difference of the images [43], then were smoothed using quadratic penalized weighted least square

method with second order difference roughness penalty [44]. Those initial field maps were improved by applying the spatio-temporally regularized reconstruction (chapter III). In the spatio-temporally regularized reconstruction, the field maps from 8 shot rosette images were used as the initial field maps for the reconstruction system models. The improved field maps were estimated via linear least square fit of the phase of the reconstructed subimages. The number of segments was 24, and the spatial regularization factor was 1 and the temporal regularization factor was 100 for all slices.

Measurement of $E_z(t)$

The through-slice dephasing due to G_{sm} was measured by two separate single-shot single-slice scans of the imaging volume with and without G_{sm} . In the scans, the rosette readout gradients were not played, so that the FID signals could be recorded. Rewriting the equation 2.1 for the FID signals, the received signals are

$$(2.6) \quad \begin{aligned} S_a(t) &= E_z(t) \cdot e^{-i\gamma(G_{sm}t+\phi_0)z_0} \iint M_2(x, y) e^{-i\omega(x, y)t} dx dy \\ S_b(t) &= \iint M_2(x, y) e^{-i\omega(x, y)t} dx dy, \end{aligned}$$

where $\omega(x, y)$ denotes the susceptibility induced off-resonance. Simply, we estimated the through-slice dephasing $E_z(t)$ by dividing $S_a(t)$ with $S_b(t)$.

Functional experiment

Following the initial field map and $E_z(t)$ measurements, two functional experiments were performed. The first functional experiment was done using a SMART acquisition. In the multi-slice excitation, the center-to-center distance between slices was designed to be 11 times of the slice-thickness, therefore the SMART sequence could cover 33 slices. G_{sm} was 0.012 G/cm, and the ω_{sm} was 165 Hz when the slice thickness was 3 mm. G_{sm} caused maximum off-resonance at the edge of the slice

profile as 15 Hz, which was well within the main peak of the spectral selectivity of the rosette trajectory. TR was 1.5 s, and TE was 30 ms, where the echo time is defined as the beginning of the rosette acquisition. The subject was required to do a bilateral finger tapping task while a visual checker board stimulation was given as a queue (20 s off/20 s on, 5 cycles). The data was reconstructed using CPSMART, ssiSMART, and iSMART reconstruction methods. The number of iterations for ssiSMART and iSMART was 10. Since the spatial resolutions of each reconstruction method are found to be different, first, each reconstruction was done at the best spatial resolution for direct comparison of the reconstructed images. Then the spatial resolution of CPSMART and ssiSMART were matched to that of iSMART for functional analysis. For CPSMART, the k-space samples at higher spatial frequency were truncated to give the spatial resolution close to that of iSMART. For ssiSMART, the spatial regularization parameter was set to 10 to match the resolution with iSMART. The cutoff frequency for CPSMART and the spatial regularization parameter of ssiSMART were determined by comparing the FWHM of the point spread function. For each image set, the functional data analysis was performed using FSL [45] software package. Using the generalized linear model, the z-score of each time course was calculated and thresholded ($p=0.05$) to determine the activation. In addition, the time-series SNR was measured for each image set. The time-series SNR was measured by dividing the mean in the ROI by the standard deviation over time in the same ROI for each slice, then by averaging them for each reconstruction method.

The second functional experiment was performed using a single slice gradient echo rosette sequence with conventional single slice excitations. The same volume coverage was prescribed as SMART experiment, however the TR had to be increased to 3.5 s. TE was 30 ms, and the slice thickness was 3 mm. The same human subject was

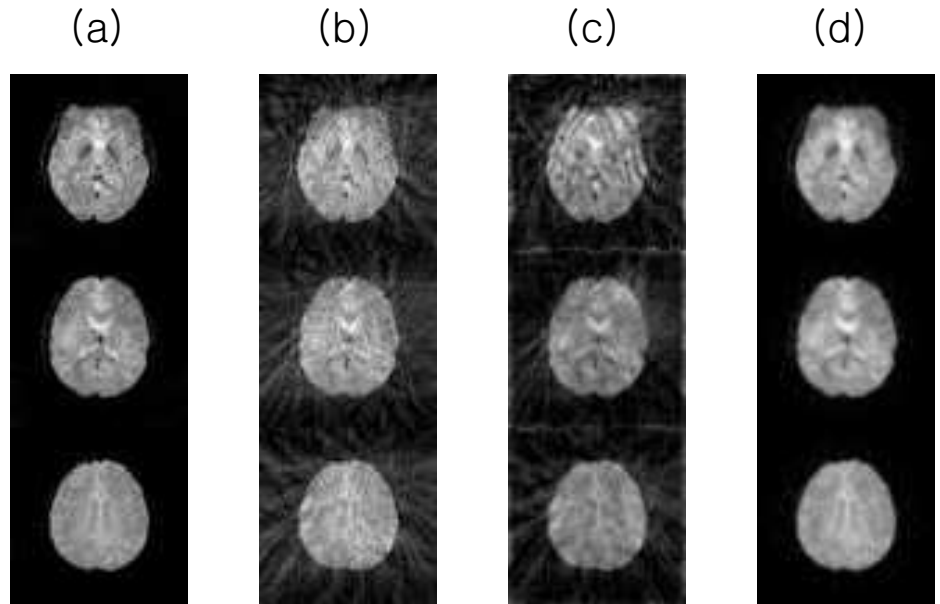


Figure 2.5: Simulation results : (a) the reference discrete object (b) the conjugate phase reconstruction (c) the iterative single slice reconstruction (d) the proposed iterative SMART reconstruction

given the same functional task. Prior to the functional study, the high-order shimming and the field map measurement were performed again to adapt the changes in the off-resonance after the preceding SMART functional study. The data was reconstructed using field-corrected iterative reconstruction [19]. The spatial regularization parameter of the iterative reconstruction was set to 10 to match the spatial resolution of iSMART images. FSL software package was used for functional data analysis. Same threshold as the previous functional analysis was used to determine the activated pixels.

2.4 Results

Figure 2.5 compares the reconstructed SMART images using CPSMART, ssiSMART, and iSMART in simulations. As was shown in [2], the conventional CPS-

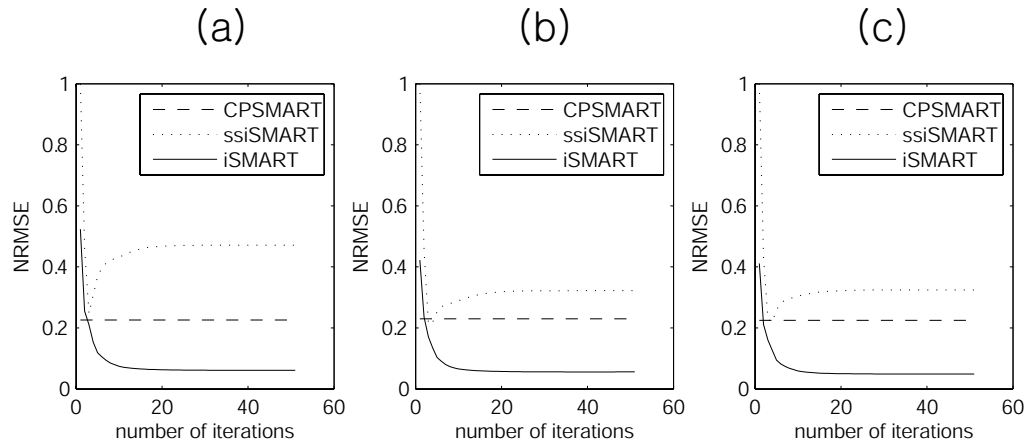


Figure 2.6: NRMSE of each reconstruction methods. The error was measured inside of the object.
 (a) slice 1 (b) slice 2 (c) slice 3

	CPSMART	ssiSMART (10 iterations)	iSMART (10 iterations)
Slice 1	0.23	0.43	0.074
Slice 2	0.23	0.29	0.066
Slice 3	0.22	0.31	0.059

Table 2.1: Simulation result : NRMSE of the reconstructed images. NRMSE was measured in the support illustrated in figure 2.4.

MART images show the noisy artifacts over the FOV. Similarly, the iteratively reconstructed ssiSMART images suffer the off-resonance artifacts originated from the other slices, while the artifacts are smooth due to the spatial regularization. In contrast, the off-resonance artifacts are significantly reduced in iSMART images. Figure 2.6 shows another evidence for the superior reconstruction results of iSMART. The NRMSE was measured in each slice at each iteration, and compared with CPSMART. Within 10 iterations, iSMART reduced about 70 % of the reconstruction error (table 2.4). Note that NRMSE is measured within the object, and measuring the error over the entire FOV would exaggerate the contrast between the two methods.

From figures 2.5 and 2.6, ssiSMART turned out to be worse than CPSMART method in spite of the reduction of artifacts outside of the object. This is because the ssiSMART reconstruction cannot distinguish between the susceptibility induced off-resonance and the off-resonance imposed by G_{sm} . The reconstruction system model does not have the G_{sm} term, and this hinders the optimization algorithm from finding the right solution. In general, as the amplitude of the susceptibility induced off-resonance approaches ω_{sm} , ssiSMART resulted worse reconstruction results. When there is no off-resonance (i.e. $\omega_1 = 0$, $\omega_2 = 0$, and $\omega_3 = 0$), ssiSMART outperformed the noniterative CPSMART method.

The iterative methods were found to be more sensitive to the error in the measured field maps that were used in the field-map corrected reconstruction. Figure 2.7 shows that both iterative methods have higher sensitivity to the error in the field map than the non-iterative CPSMART method. As the RMSE of the field map reaches 20 Hz, the quality of iSMART images reaches more than 100% reconstruction error. Therefore, use of a good high order shimming and accurate field map estimation method are essential to iSMART method.

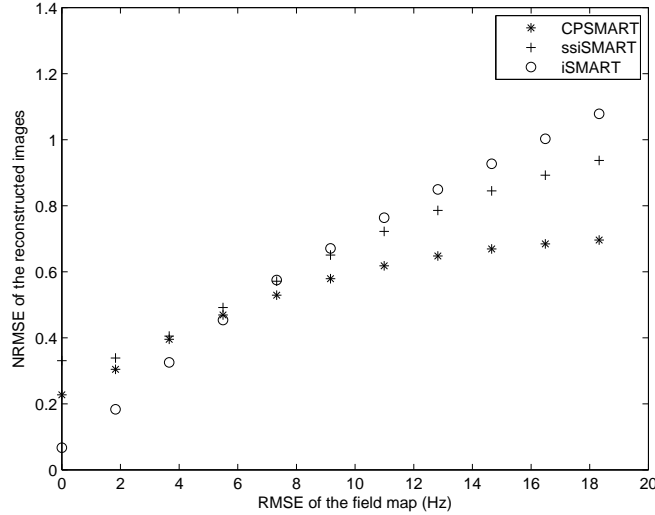


Figure 2.7: Sensitivity of each reconstruction method to the field map errors

Figure 2.8 (a) shows that the point spread function of iSMART reconstruction is wider than the other methods. This is due to the severe sparse sampling of k-t space in the SMART acquisition. The FWHM of the point spread function was found to be 1.2 pixels for CPSMART, 1.3 pixels for ssiSMART, and 1.5 for iSMART. Figures 2.8 (b) ~ (d) show the center profile of the point spread functions of all slices for each reconstruction method. As expected, the perturbation in slice 2 caused artifacts in the other slices, while iSMART has the lowest artifacts.

Figure 2.9 shows the reconstruction results for a human subject. Note that figure 2.9 (a) required 3 TRs while (b) ~ (d) required only 1 TR. As was seen in the simulation results, iSMART reduced most of the off-resonance artifacts in the slices for the price of smoother images. The same functional data set was re-reconstructed matching the spatial resolution of CPSMART and ssiSMART to that of iSMART. Figure 2.10 shows the activated pixels overlaid the reconstructed images after matching the spatial resolution. Figure 2.10 (a) shows the activations from single-slice excitation experiment, and (b) ~ (d) show that three methods are equivalent to the

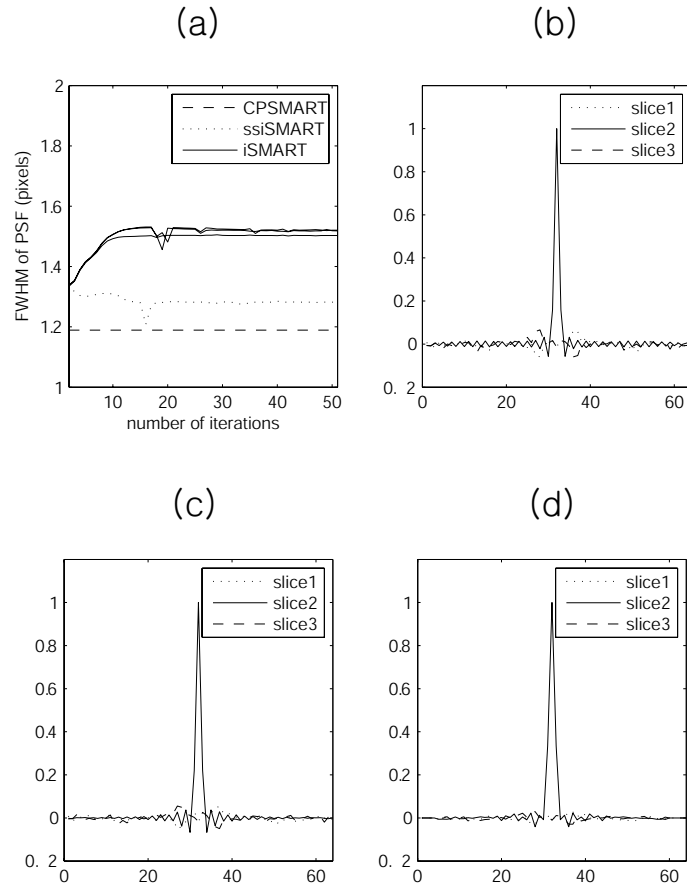


Figure 2.8: (a) The FWHM of the point spread function of each reconstruction method. Center profiles of the point spread functions of the on-resonant slice (slice 2) and the off-resonant slices (slice 1 and 3): (b) conjugate phase (CPSMART) reconstruction (c) iterative single slice (ssiSMART) reconstruction (d) iterative SMART (iSMART) reconstruction.

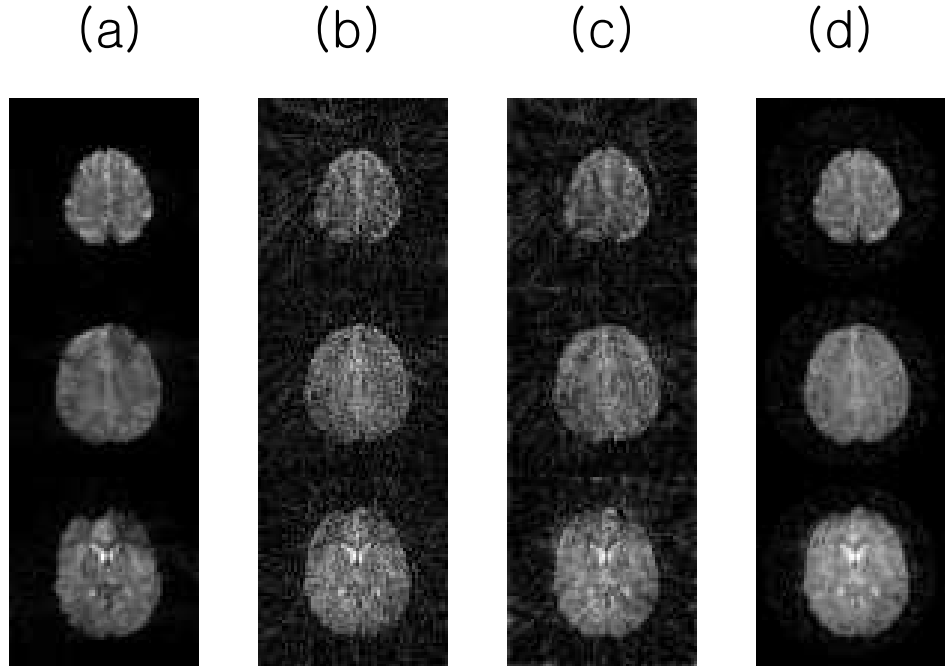


Figure 2.9: (a) Reconstructed images from a single slice acquisition. (b) CPSMART reconstructed images from SMART acquisition. (c) ssiSMART reconstructed images from SMART acquisition. (d) iSMART reconstructed images from SMART acquisition.

single slice excitation in terms of the activation areas. Comparing figures 2.10 (b) \sim (d), iSMART resulted more activation areas. However, comparing all 33 slices reconstructed, iSMART did not always result in the largest activated areas (figure 2.11). The time-series SNR were 18.5 for iSMART, 15.4 for cpSMART, and 18.0 for ssiSMART.

2.5 Discussion

In this chapter, we demonstrated that iSMART method can reduce most of the off-resonance artifacts which is prevalent on the conventional CPSMART reconstruction. However, the method required very accurate system model for a satisfactory results. In the following, we discuss some of the factors that could affect the iterative method.

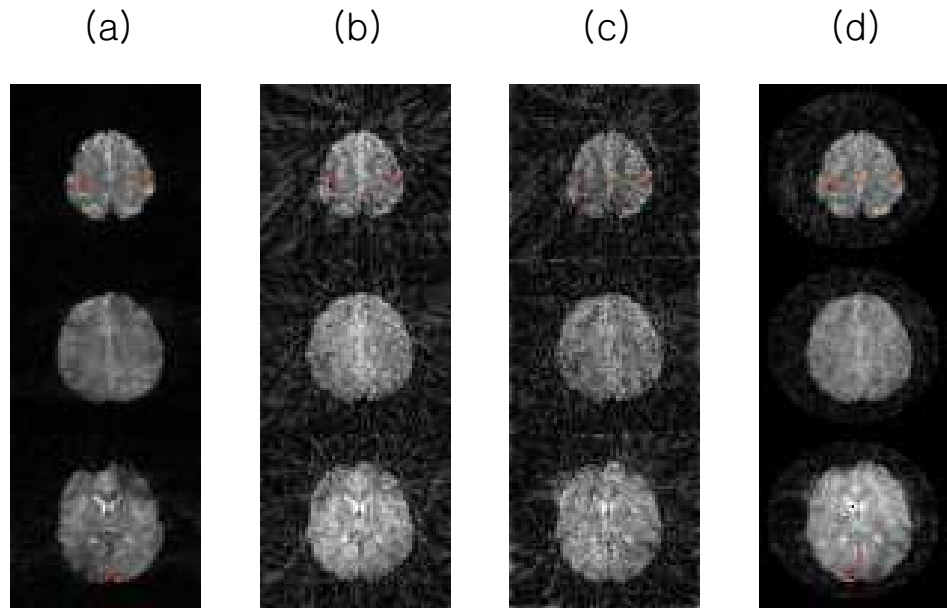


Figure 2.10: (a) Activation maps from single slice acquisition. (b) Activation maps from CPSMART reconstruction of SMART acquisition. (c) Activation maps from ssiSMART reconstruction of SMART acquisition. (d) Activation maps from iSMART reconstruction of SMART acquisition.

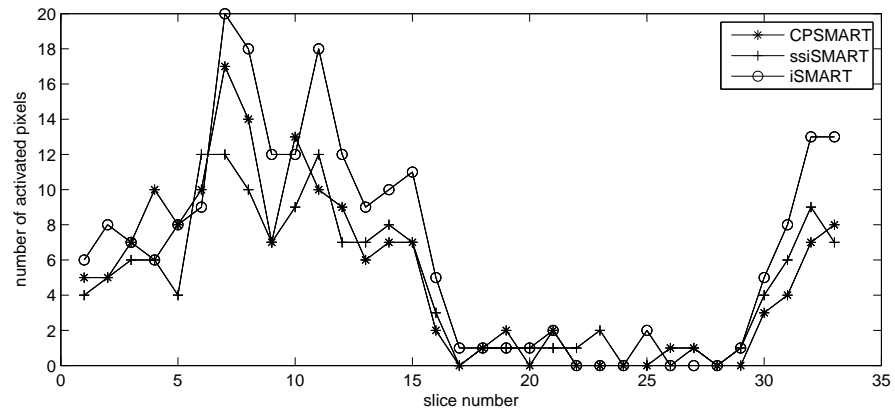


Figure 2.11: The number of activated pixels for each slice ($p=0.05$). Slice 1 denotes the superior side of the imaging volume.

Spatial regularization

In the system model (equation (2.3)), many terms need to be determined before applying the conjugate gradient method. First of all, the sampled data set is contaminated by the complex white Gaussian noise, which is mainly from the thermal noise in the object. In 3T GE scanner, the typical signal to noise ratio is 100 to 1. At this noise level, the iterative reconstruction can result in a noisy image after certain number of conjugate gradient iterations. The noisiness of the reconstructed object can be reduced by the roughness penalty added in the cost function. However, increasing the weight in the roughness penalty, i.e. increasing β in the equation (2.4) leads to more bias in the reconstructed images for the price of less noisiness. The time-series SNR was higher in both iSMART and ssiSMART than cpSMART. Obviously, the spatial regularization also helped to increase the time-series SNR, therefore increasing the detectability of fMRI study.

System model accuracy

The susceptibility induced off-resonance should be measured for a proper correction in the iSMART reconstruction. The importance of achieving very high accuracy (RMSE less than 5 Hz) needs to be stressed, since both spectral selectivity of rosette trajectories and the ill-conditionedness of SMART reconstruction increase the sensitivity to the field map error very much. In our human experiment, using the field map from 8 shot rosette images introduced some uncorrected artifacts in the iSMART images. However, as shown in the results section, using the field maps improved by the spatio-temporally reconstruction reduced most of the remaining off-resonance artifacts. For more or similar accuracy in the field map, one could also use more number of shots. However, more number of shots involves more scan time, and the accuracy of the measurement can be affected by subject motion, respiration, or scanner drift.

Other trajectories such as spiral, which is more robust to the off-resonance, could be used in the field map measurement. However, in this work, it was not done for implementation convenience.

The through-slice dephasing, $E_z(t)$ was measured for couple of reasons. First, the gradient-time area of prephasing gradient blip, or ϕ_0 , can be inaccurate because of insufficient eddy current correction. Second, imperfect slice profile can cause deviation of $E_z(t)$ from a sinc function. Because the imperfection of $E_z(t)$ is caused mostly by the scanner characteristics, a parameterized estimation of $E_z(t)$ with more realistic slice profile would be helpful to get rid of the necessity of measuring $E_z(t)$ at every scan. $E_z(t)$ also can have spatial variation due to the susceptibility induced off-resonance. A more accurate system model would have to include the spatial dependency of $E_z(t)$.

The effect of the k-space trajectory error was not investigated in this work. The accuracy could be further increased by using measured k-space trajectory. However, the benefit seems to be marginal, as the iSMART images using designed trajectory turned out to be reducing most of the artifacts.

The computational cost of iSMART is comparable to the conventional single slice iterative reconstruction, since iSMART requires only extra $O(M)$ additions for the forward and back projections in CG algorithm.

Future work

Our choice of rosette trajectory was simply by trial and error. A more careful, and automated way is conceivable such as optimization of a rosette trajectory using genetic algorithm [46]. One could also think of increasing the number of slices that are excited simultaneously. In this work, the number of k-space data samples was nearly 11,000, while the number of unknowns was about 7,400. Therefore, with one

more slice, the problem is still over-determined. However, adding one more slices could increase sensitivity of the reconstruction to the system model error such as field maps, and T_2^* decay. It might suffer from further reduction in spatial resolution. A slight increase of readout would be helpful.

Another natural extension of the method is combining it with parallel imaging techniques. The iSMART reconstruction allows an easy extension of the system model to the parallel imaging [41, 42]. Using the extra information of sensitivity maps of array coils, the acquisition length can be reduced. However, the method may suffer from extra system model error in the measured sensitivity maps. Therefore, developing a very accurate way to measure sensitivity map will be an essential step to this extension. There are other parallel imaging methods that do not need an estimation of sensitivity map. For example, a short auto calibration scan data is used to calculate the missing data points in k-space (GRAPPA) [47]. This method was originally developed for Cartesian sampling scheme, and adaptation into non-Cartesian trajectories can be done [48, 49].

2.6 Conclusion

In this chapter, we introduced the iterative SMART reconstruction method, which significantly reduced the off-resonance artifacts. A comparison study between iSMART and the conventional CPSMART revealed that the proposed method reduced the reconstruction error for the price of slightly reduced spatial resolution and increased computation. To achieve high accuracy in the reconstruction, the proposed method required measured field map and the through-slice dephasing term with very high accuracy. One functional study result was shown to demonstrate that the proposed reconstruction produced more activated pixels in most of the slices, and

resulted higher time-series SNR.



CHAPTER III

A robust, dynamic R_2^* -and-field-map-corrected image reconstruction for single shot self-refocusing trajectories at 3T

3.1 Introduction

Self-refocusing trajectories are defined as those k-space trajectories that sample the origin of k-space multiple times, forming multiple gradient echoes. Self-refocusing trajectories include multi-echo projection reconstruction (PR) trajectories [50, 51], and rosette trajectories [2, 11].

Multiple visits to the origin of the k-space cause the reconstructed images to be sensitive to off-resonance effects. This property is known as spectral selectivity in the literature on the rosette trajectories, and it is shared by other self-refocusing trajectories. Noll et al. used the spectral selectivity of rosette trajectories to selectively reconstruct different chemical species or multiple slices with different resonant frequencies [2, 11].

However, this property can create difficulties in image reconstruction for high field imaging. If the off-resonance frequency is high enough to move an image voxel out of the pass band of the spectral selectivity, the image intensity at the voxel will be significantly reduced. In this case, the artifact from field inhomogeneity is mainly local signal loss, rather than blurring in spiral imaging or geometric distortion in EPI

(Echo Planar Imaging). The signal loss is exacerbated when single shot method is used, because the width of the pass band is inversely proportional to the acquisition length [2].

It is also known that R_2^* (or $1/T_2^*$) decay during the readout can cause streaking artifacts and blurring, if it is not accounted for in the reconstruction [51].

A standard approach to reduce the R_2^* and off-resonance artifact is to use fewer echo trains, or to use multi-shot methods. Conventionally, the acquisition time for an echo train is restricted to ensure relatively small magnitude and phase changes from R_2^* and off-resonance. However, this method can increase scan time, making it more susceptible to physiological noise and subject motion.

Another approach to reduce the artifact is to incorporate the off-resonance and/or R_2^* map in the reconstruction model [2,11,51,52]. However, these methods depend on accurate pre-estimates of off-resonance and/or R_2^* maps. Due to the limited accuracy of the low resolution maps estimated from the same data, the acquisition length was still restricted to nine echoes [51], or the spatial resolution and field of view had to be reduced [2]. In addition, in high field imaging, it is often difficult to derive a field map for lower brain slices from single shot data, since the large off-resonance there leads to insufficient signal or significant distortion.

In this chapter, we propose a spatio-temporally regularized iterative reconstruction method as a new approach to correct for the R_2^* and off-resonance artifacts in single shot self-refocusing trajectories. This method can accurately reconstruct R_2^* -and-field-map-corrected images for the single shot PR and rosette trajectories at 3T. It does not require a pre-determined R_2^* map, and only requires the initial guess of a low accuracy field map. Beyond the R_2^* -and-field-map-corrected reconstruction, the subimages generated by the method can be used in dynamic estimation of accurate

R_2^* and field map by fitting the magnitude and phase time courses of each voxel to a complex exponential model.

Dynamic field mapping can improve image quality, for example, by capturing the fluctuation of the main field during functional imaging studies. Such fluctuations are caused by head movement, passive shim heating, and respiration [53]. The proposed method is suitable for addressing such fluctuations.

Dynamic R_2^* mapping has been used in a variety of MR applications [8,9,54–57]. In functional MRI, dynamic R_2^* mapping provided nearly optimal functional contrast and activation volume [58], and better contrast to noise ratio than T_2^* -weighted imaging [8]. R_2^* is more closely linked to physiological parameters in functional MRI, which may allow for better inter-subject and inter-tissue comparisons, and the measurement can be more independent of scan parameters and hardware fluctuations.

Recently, there have been several studies that tried to estimate the field map and/or R_2^* map along with the proton density image, I_0 , simultaneously from a single-shot gradient echo data, using trajectories such as spiral-in and out, multi-echo EPI, or rosette [53, 59, 60]. However, these methods were not able to address R_2^* decay [53], required high computational cost [59], or could detect only relatively small R_2^* changes between acquisitions via linearization [60]. Our proposed method estimates R_2^* decay and field map simultaneously without assuming small R_2^* changes.

In the following sections, we introduce a mathematical description of the proposed method, and a strategy to obtain the initial field map from single shot data. We also present an approach to determine the regularization parameters throughout simulations, as well as the functional imaging results. All simulations were conducted using both PR and rosette trajectories, while experiments were performed using single shot rosette trajectories.

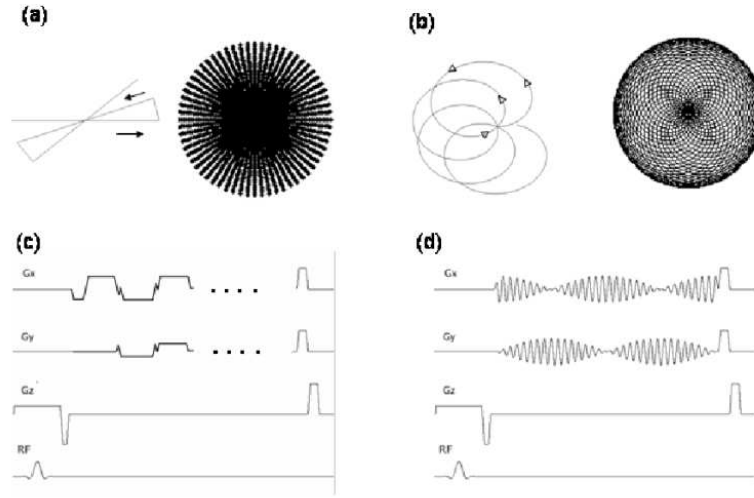


Figure 3.1: (a) Single shot PR trajectory (sequential view ordering) (b) single shot rosette trajectory (c) single shot PR pulse sequence (d) single shot rosette sequence

3.2 Theory

3.2.1 Self-refocusing trajectories and their R_2^* and off-resonance artifacts

The main difference between PR and rosette trajectory is the number of self-crossing points. The self-crossing point of PR is located only at the origin of k-space. In rosette trajectories, the number of self-crossing points can be controlled via the ratio between two frequencies ω_1 and ω_2 , where the trajectories are described as [2]

$$(3.1) \quad \vec{k}(t) = \sin(\omega_1 t) e^{i\omega_2 t}.$$

Figure 3.1 shows examples of PR and rosette trajectories and corresponding pulse sequence diagrams.

If there is unwanted off resonance, the reconstructed images can lose intensity severely due to the spectral selectivity. In addition, R_2^* decay causes artifacts in the reconstruction unless it is properly addressed.

In the following section, we propose a spatio-temporally regularized iterative reconstruction method that can correct for the artifact from R_2^* and field map simultaneously.

3.2.2 Iterative image reconstruction with spatio-temporal regularization

The baseband signal $S(t)$ of MR with mono-exponential T_2^* (or $1/R_2^*$) decay can be modeled as [4]

$$(3.2) \quad S(t) = \int f_0(\vec{r}) e^{-R_2^*(\vec{r})t} e^{-i\omega(\vec{r})t} e^{-2\pi i \vec{k}(t) \cdot \vec{r}} d\vec{r}, \quad \tau_1 \leq t < \tau_{end},$$

where $f_0(\vec{r})$ is the transverse magnetization at the beginning of the data acquisition; $R_2^*(\vec{r})$ is the R_2^* map in sec^{-1} ; $\omega(\vec{r})$ is the B_0 field inhomogeneity; \vec{r} is the spatial location vector; and τ_1 and τ_{end} are the beginning and the end of the acquisition respectively.

Assuming that the R_2^* decay is negligible during the l th time segment, $\tau_l \leq t < \tau_{l+1}$, we can rewrite (3.2) as

$$(3.3) \quad S_l(t) \approx \int f_l(\vec{r}) e^{-i\omega(\vec{r})t} e^{-2\pi i \vec{k}(t) \cdot \vec{r}} d\vec{r}, \quad \tau_l \leq t < \tau_{l+1}, \text{ and } l = 1, \dots, L,$$

where L denotes the number of data segments, and $f_l(\vec{r}) = f_0(\vec{r}) e^{-R_2^*(\vec{r})TE_l}$ is the l th *subimage* with the echo time TE_l . We define TE_l as the beginning of each segment, $TE_l = t_l$, and each segment has approximately equal size.

We discretize (3.3) in a matrix-vector form with additive complex white Gaussian noise $\epsilon \in \mathbb{C}^{M_l \times 1}$ as

$$(3.4) \quad \mathbf{Y}_l = \mathbf{A}_l \mathbf{X}_l + \epsilon,$$

where $\mathbf{Y}_l \in \mathbb{C}^{M_l \times 1}$ is the l 'th segment of the measured complex MR signal; M_l denotes the number of data samples in the l th segment; $\mathbf{X}_l \in \mathbb{C}^{N \times 1}$ is the l th discrete subimage i.e., $[\mathbf{X}_l]_n = f_l(\vec{r}_n)$; and $\mathbf{A}_l \in \mathbb{C}^{M_l \times N}$ is the l th system matrix. The elements of \mathbf{A}_l are

$$[\mathbf{A}_l]_{mn} = e^{-i2\pi \vec{k}(t_m) \cdot \vec{r}_n} e^{-i\omega(\vec{r}_n)t_m}, \quad m = 1, \dots, M_l \text{ and } n = 1, \dots, N,$$

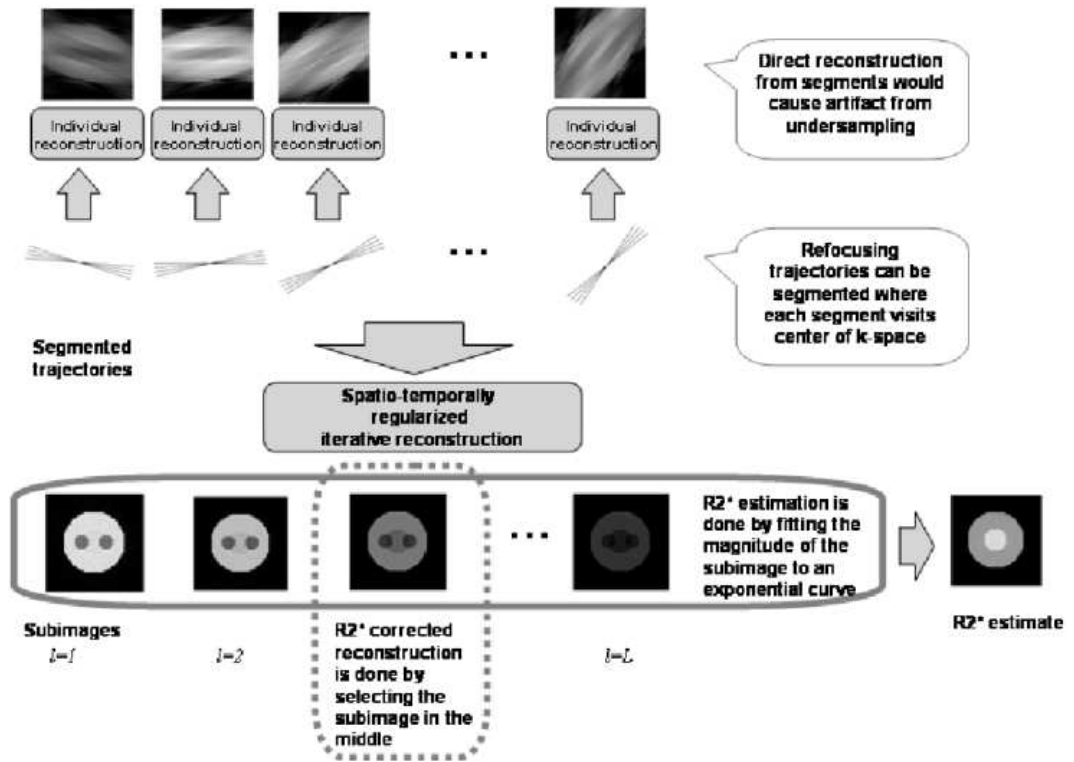


Figure 3.2: The proposed R2* corrected reconstruction scheme (dotted line) and dynamic R2* estimation (solid line)

where $\hat{\omega}$ is an initial guess of the field map.

To ensure minimal signal change due to R_2^* decay, the length of each segment should be much smaller than T_2^* , i.e., a few milliseconds. If the individual subimages were directly reconstructed from each data segment, there would be artifacts from high levels of undersampling (Figure 3.2). To overcome the limited k-space coverage of each segment, additional information on the subimages is necessary.

In previous work, we used temporal evolution of the subimages based on the complex exponential model as the additional information to reduce the undersampling artifacts. The complex exponential model included the pre-estimated R_2^* map and the field map [61]. An extra penalty term penalized the subimages against the complex model, where the term was added to the cost function of iterative penalized

least square reconstruction [62].

In this chapter, we propose to penalize the second derivative of the time course of subimages. This temporal regularization is adequate to capture the temporal evolution of the magnitude and phase of the subimages. There are advantages to this temporal regularization scheme compared with our previous work. First, the new regularization scheme does not require the preestimation of R_2^* map. Second, it is more robust to the errors of the initial field map used in the reconstruction. Third, it is not limited to the mono-exponential model; instead it allows models with smoothly varying functions.

In the proposed regularization scheme, the penalty term is modified to regularize the second derivative of the temporal evolution of the subimages, which represent the object corresponding to each data segment. The final cost function ϕ consists of the data fit term, spatial regularization term for each subimage, and the temporal regularization term as

$$(3.5)\phi = \sum_{l=1}^L \|\mathbf{Y}_l - \mathbf{A}_l(\hat{\omega})\mathbf{X}_l\|^2 + \beta \sum_{l=1}^L \|\mathbf{C}\mathbf{X}_l\|^2 + \gamma \sum_{l=2}^{L-1} \|\mathbf{X}_{l-1} - 2\mathbf{X}_l + \mathbf{X}_{l+1}\|^2,$$

where \mathbf{C} is a spatially differencing matrix for the spatial smoothness penalty; β is the spatial regularization parameter; and γ is the temporal regularization parameter. The reconstruction of subimages is done by minimizing ϕ over the subimages \mathbf{X}_l 's as follows:

$$(3.6) \quad (\hat{\mathbf{X}}_1, \hat{\mathbf{X}}_2, \dots, \hat{\mathbf{X}}_L) = \underset{\mathbf{X}_1, \mathbf{X}_2, \dots, \mathbf{X}_L}{\operatorname{argmin}} \phi(\mathbf{X}_1, \mathbf{X}_2, \dots, \mathbf{X}_L; \hat{\omega}).$$

In our experiment, we used the conjugate gradient iteration for minimization. Assuming that each time segment is sufficiently small, we model the reconstructed subimages $\hat{\mathbf{X}}_l$ as

$$(3.7) \quad [\hat{\mathbf{X}}_l]_n = f_l(\vec{r}_n) e^{-i(\omega(\vec{r}_n) - \hat{\omega}(\vec{r}_n))TE_l}.$$

From the magnitude of \mathbf{X}_l 's, we can estimate the R_2^* map by fitting to an exponential curve. If it is necessary, one can estimate the field map residual $\omega(\vec{r}) - \hat{\omega}(\vec{r})$ using a log-linear fit of the phase of subimages, and use the refined field map to re-estimate the subimages. However, the convergence of such an iteration is not guaranteed, and our preliminary simulation results show that there is only minimal improvement from reestimation with an updated field map. Figure 3.2 illustrates how the spatio-temporal regularized iterative reconstruction is done.

3.2.3 R_2^* -and-field-map-corrected reconstruction

Ideally, every subimage \mathbf{X}_l reconstructed from the iterative scheme described in the previous section is R_2^* corrected, since the data segment size is small enough not to allow significant R_2^* decay in each of them. However, due to the structure of the temporal regularization and finite length of the acquired data, the first and last subimages have fewer neighbors to regularize with. This results in more artifacts in the subimages in near the boundary of data acquisition than the subimages in the middle of data acquisition.

Therefore, we simply choose the middle (L/2th) subimage among the subimages from the spatio-temporally regularized iterative reconstruction as the R_2^* -and-field-map-corrected image. The basic outlines of the procedure is described as dashed lines in Figure 3.2.

3.2.4 R_2^* and field map estimation from extended data set

The R_2^* map is estimated by least-square fitting the magnitude of the low-reconstruction-error subimages to a mono-exponential curve. Similarly, the field map is estimated from the sum of the initial field map and the log-linear fit of the phase of the subimages. In this procedure, we used the first half of the subimage sequence

reconstructed from the spatio-temporally regularized iterative reconstruction.

Extending data acquisition results in more accurate R_2^* and field maps, since it has less proportion of subimages which are affected from the boundary effect. On the other hand, the length of acquisition is limited by hardware capability and the MR signal strength. Therefore, the length of extended data acquisition needs to be determined within those limitations. Figure 3.2 again illustrates the basic scheme of this procedure.

To get accurate estimates of \mathbf{X}_l 's, a few unknown terms in (3.6) must be predetermined. The following sections explain how to determine the initial field map and the design parameters.

3.2.5 The estimation of initial field map

Off resonance effects cause phase changes between the neighboring subimages. If the phase change is too large, the temporal regularization can reduce the difference in phase more than the difference in the magnitude. This causes artifacts in the subimages, and results in erroneous estimation of the R_2^* and field maps.

To avoid large phase changes, the *safe range* of the off-resonance can be defined as follows. Assuming that the time difference between neighboring subimages is about 4ms, the off-resonance cannot cause more than $\pi/4$ of phase difference during that period. Therefore the maximum allowable off-resonance will be 31Hz. We call this interval of off-resonance as the *operation range* of the temporal regularization for given length of data segment.

At 3T, the off-resonance frequency often exceeds 31Hz even with good shimming procedures. This is why the initial field map $\hat{\omega}$ is necessary in the proposed method. As is denoted in (3.7), the phase evolution of the estimated images depends on the difference between the unknown true field map and the initial field map. If the

field map error is smaller, i.e. less than 31Hz, the spatio-temporally regularized reconstruction will result in less artifacts in the subimages.

On the other hand, for single-shot-self-refocusing trajectories at 3T, it is often difficult to achieve small error in the field map using the standard 'two-point' method [63]. The images with delayed echo time, which are to be used in estimating the field map, suffer severe image intensity loss due to the spectral selectivity. For example, a 25Hz of off-resonance will cause significant loss of image intensity for 40ms-long single-shot rosette acquisition, since the FWHM (Full Width Half Maximum) of spectral selectivity is the inverse of acquisition length [11].

To estimate the initial field maps with errors within the *operation range* of the temporal regularization for single-shot-self-refocusing trajectories at 3T, we improved the 'two-point' method to ignore incoherent data points in the reconstruction of images with different echo times. We choose a grid in an area near the center of k-space, reconstruct low resolution images at different echo time using only first data point that visits each grid point. Using this method, from a pair of rosette data with echo time difference of 2.5ms, we estimated a field map with the RMSE (Root Mean Squared Error) 6.79Hz, where the maximum absolute off-resonance of the true field map was 80.4Hz. Figure 3.3 compares the field maps from the standard 'two-point' method and our improved method.

3.2.6 Determining the design parameters

Spatial regularization is known to introduce a trade off between spatial smoothness and image noise variance [24]. High β s would result in the loss of the spatial resolution of the subimages \mathbf{X}_l s and the estimated R_2^* map, while low β s would cause unwanted amplification of the noise. The temporal regularization parameter γ has similar effect in the temporal direction. Excessive temporal regularization would cause the time

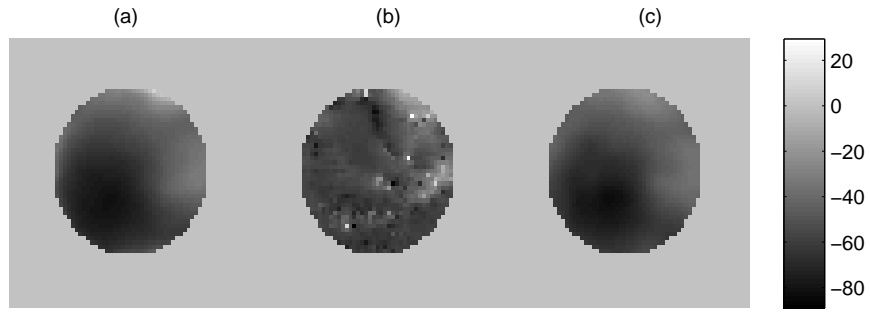


Figure 3.3: (a) The reference field map. (b) Estimated field map from conventional 'two-point' method (RMSE = 14.23Hz, Max error = 98.5Hz). (c) Estimated field map from the proposed field map estimation method (RMSE = 3.43Hz, Max error = 34.46Hz).

course of subimages resemble a straight line, introducing bias in the R_2^* estimates with less variance. On the other hand, low temporal regularization would bring in more undersampling artifact in the subimages, which will introduce noisy time course of subimages.

The number of segments L and the total data length play an important role in the accuracy and the speed of the reconstruction. For a given length of data, one could choose very large L to reduce the approximation error of R_2^* decay during each data segment. However, smaller data segments will introduce more undersampling artifact despite temporal regularization, and require more memory and computation time.

Choosing the right set of design parameters is another challenging task. In this work, we determined the design parameters given a data set in simulations and experiments. Section 3.3 describes how this was done.

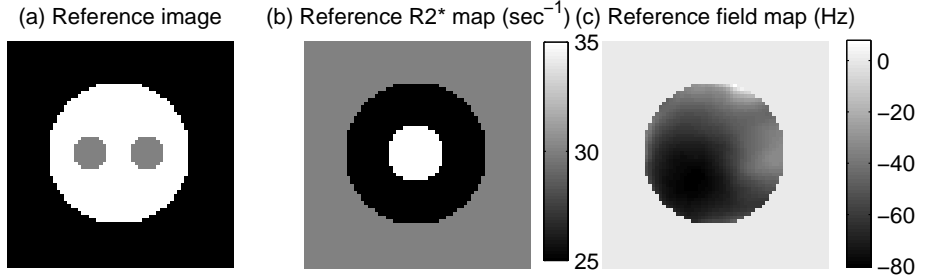


Figure 3.4: The reference image (a), R_2^* map (b), and field map (c) used in simulations

3.3 Simulations

3.3.1 Method

The simulations were conducted using 64×64 discrete image, R_2^* map and field map as shown in Figure 3.4. The k-space data was generated using direct implementation of equation (3.4) without noise. We implemented the reconstruction based on the NUFFT (NonUniform Fast Fourier Transform) representation of the MR system matrix ¹ [19] in MATLAB (Mathworks Inc. Natick, MA). 300 iterations were used for all simulations.

The PR and rosette trajectories shown in Figure 3.1 were used with variations in the number of extra spokes or petals. PR trajectories had 128 spokes for the estimation of the R_2^* and field maps, and 64 spokes for R_2^* -and-field-map corrected reconstruction. Each spoke had 128 samples, and the sampling time was $4\mu\text{s}$. For simplicity, no transition time between the spokes was assumed for simplicity.

Rosette trajectories had the fast radial frequency $\omega_1/2\pi=1.087$ kHz, and slow angular frequency $\omega_2/2\pi=113.22$ Hz. For R_2^* -and-field-map corrected reconstruction, these choices led to 48 cycles of radial oscillation, and for R_2^* -and-field-map estimation, the extended trajectory had 96 cycles of radial oscillation. The readout lengths of the rosette trajectories were 44.4ms and 88ms respectively with sampling time

of $4\mu\text{s}$. The time segmentation of trajectory was done carefully so that each segment had almost the same number of spokes or petals. For rosette trajectories, each segment started from the center of the k-space.

3.3.2 Determining the design parameters

The design parameters were determined by simulations. Using the synthesized k-space data, the subimages were reconstructed with a range of β , γ , and L values. For these simulations only, the reference field map was used as the initial field map, since this choice should provide the best achievable reconstruction performance. For each reconstruction, the NRMSEs (Normalized Root Mean Squared Error) of the magnitude subimages with respect to the R_2^* -weighted reference images were measured, and the minimum values of the NRMSEs were compared for various values of the design parameters.

Figure 3.5 shows the minimum NRMSEs for the various values of β , γ , L and acquisition length. The β and γ values that gave the minimum reconstruction error depended on the length of segment rather than the acquisition length or L . In addition, the overall NRMSE was lowest when each segment included two spokes or petals.

From the simulations, the best spatial regularization parameter β was chosen as 1, the temporal regularization parameter γ was 400, and the number of data segments L was 32 for the PR trajectory of 64 spokes.

We also performed similar simulations for the rosette trajectories (not shown).

3.3.3 R_2^* -and-field-map-corrected image reconstruction

For comparison, we performed four different simulations. First, we reconstructed the field-map-corrected T_2^* -weighted image using fast iterative reconstruction [19]. In

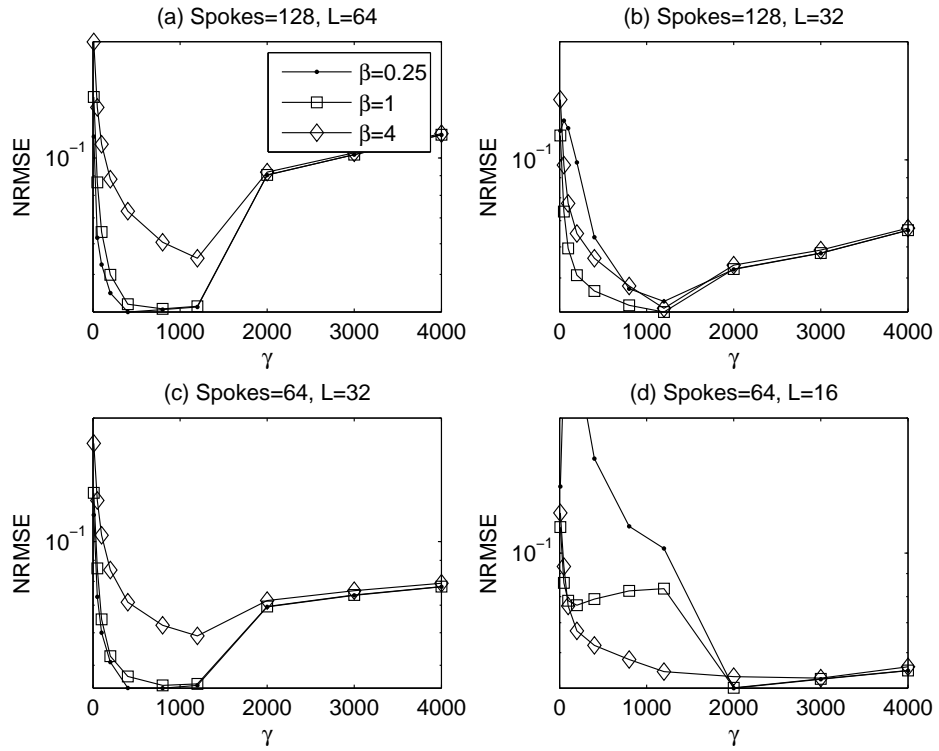


Figure 3.5: The minimum NRMSE of subimages with different β and γ values for various data lengths and numbers of segments.

this method, we used the reference field map in the reconstruction system model to highlight the artifact from R_2^* decay during the data acquisition (Figure 3.6 (a)). Second, instead of the reference field map, we used the initial field map estimated from the method described in section 3.2.5. The standard fast iterative reconstruction reveals that the estimation error of the initial field map causes significant amount of artifacts in the reconstructed image (Figure 3.6 (b)). Third, the initial field map was also used in the proposed R_2^* -and-field-map-corrected reconstruction (Figure 3.6 (c)), and the reference field map was again used in the proposed R_2^* -and-field-map-corrected reconstruction method (Figure 3.6 (d)). The design parameters determined in the previous section were used in the reconstructions. Figure 3.6 (c) and (d) indicate that the proposed R_2^* -and-field-map-corrected reconstruction method not only reduces most of the artifacts from both R_2^* decay and field map error but is also robust to the error in the initial field map. Note that the most of the remaining artifact in the proposed method (Figure 3.6 (c)) is local to the area where the error in the initial field map was highest (47.9 Hz) in the region of interest.

For rosette trajectories, we achieved similar results, where the NRMSE of no R_2^* -corrected image was 0.376, NRMSE of the field-corrected image using the initial field map was 0.369, and the NRMSE of the proposed method using the initial field map was 0.047.

3.3.4 R_2^* -and-field-map estimation

Using the design parameters determined from section 3.3.2 ($\beta=1$, $\gamma=400$, $L=64$, PR trajectory with 128 spokes), we estimated the R_2^* and field maps using the proposed method (Figure 3.7). The area where higher error in the initial field map presents showed more error in the estimated R_2^* map. The accuracy of the field map was significantly improved by the proposed R_2^* -and-field-map estimation method over

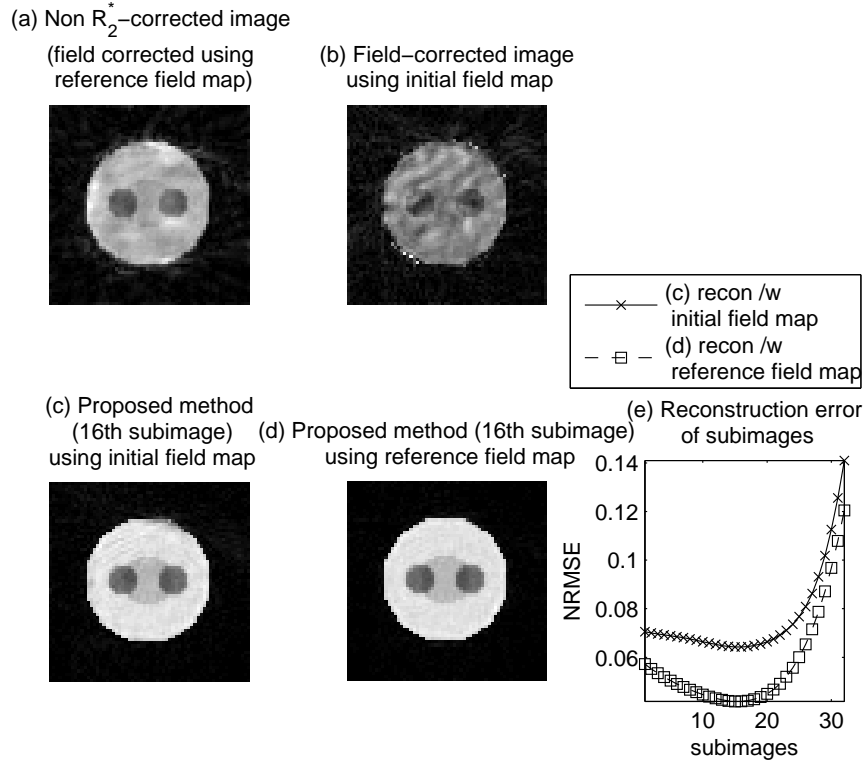


Figure 3.6: (a) Field-map-corrected image using the reference field map without R_2^* correction (NRMSE=0.28), (b) field-map-corrected T_2^* -weighted image using the initial field map without R_2^* correction (NRMSE=0.31), (c) proposed method with the initial field map (16th subimage, NRMSE=0.064), (d) proposed method with the reference field map (16th subimage, NRMSE=0.042). (e) The NRMSE of each subimage for (c) and (d). The maximum error in the initial field map was 47.9Hz with RMSE of 3.1Hz. The design parameters for the proposed method were $\beta=1$, $\gamma=400$, $L=32$.

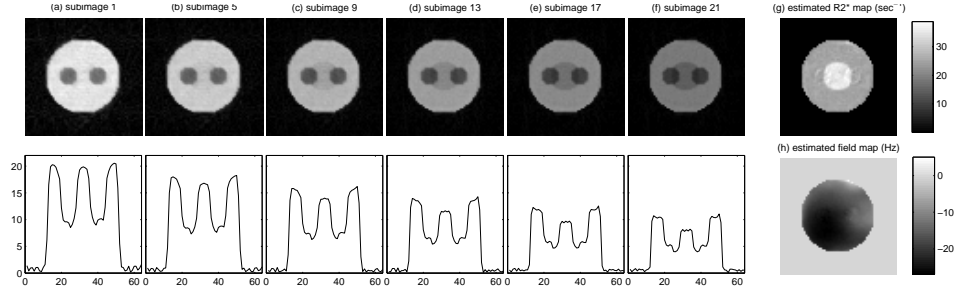


Figure 3.7: (a) (f) The subimages ($l=1,5,9,13,17,21$) and their profiles. (g) the estimated R_2^* map (RMSE = 1.32sec^{-1}) and (h) the estimated field map (RMSE = 0.52Hz).

	Initial field map		Estimated field map		Estimated R_2^* map	
	RMSE	max.error	RMSE	max.error	RMSE	max.error
Field map 1	0.86 Hz	8.02 Hz	0.52 Hz	2.99 Hz	1.32 s^{-1}	7.77 s^{-1}
Field map 2	2.27 Hz	20.50 Hz	0.68 Hz	4.34 Hz	1.97 s^{-1}	16.03 s^{-1}
Field map 3	3.27 Hz	31.71 Hz	0.91 Hz	8.73 Hz	3.11 s^{-1}	24.87 s^{-1}

Table 3.1: Estimation errors of the field maps and R_2^* maps for synthesized data sets with different field map magnitudes. Field map 3 (max amplitude = 79.1 Hz) is identical to the reference field map shown in Fig. 3.4. Field maps 1 (max amplitude = 26.4 Hz) and 2 (max amplitude = 52.7 Hz) are obtained by scaling field map 3 by 0.33 and 0.67, respectively.

using only the initial field map.

While the extended acquisition length increased the accuracy of the reconstructed subimages, it also increased the sensitivity of R_2^* map estimation to the error of the initial field map. Table 3.1 shows the result of the simulations for various values of the reference and the initial field maps. The proposed method improved the accuracy of the field maps from the initial field maps, but the accuracies of the estimated R_2^* maps were affected at the locations where the errors in the initial field maps were high.

3.4 Experiments

3.4.1 Method

All MRI data were acquired on a 3T scanner (GE Signa, Milwaukee, WI). Written informed consent was obtained from subjects prior to the MRI scan. Two MRI

experiments were performed on human subjects.

Experiment I : For the R_2^* -and-field-map-corrected image reconstruction, five measurements were acquired for twenty contiguous slices with 3mm thickness. The scan parameters were $TR = 2s$, $TE = 5ms$, and $FOV = 20cm$, where TE was defined as the beginning of the rosette acquisition. The first time point was delayed by 2.5ms to estimate the initial field map as described in section 3.2.5. The parameters for the rosette trajectory were kept the same as in the section 3.3. Total readout was 44.4ms. Each session was preceded by non slice selective fat presaturation pulse. The R_2^* -and-field-map-corrected reconstruction was done based on the design parameters determined from simulations ($\beta=1$, $\gamma=150$, $L=24$).

Experiment II : For the R_2^* -and-field-map estimation, ten contiguous slices (slice thickness = 3mm) were acquired while a functional imaging study was conducted. An 8Hz flickering checker board was used as visual stimulation to the subject, while finger tapping task was asked to be performed during the visual stimulus. The visual stimulus was presented for 5 cycles with 20s off/20s on. The scan parameters were kept the same as those used in the first experiment, and the initial field map was also estimated from the delayed acquisitions. The readout was 88ms for the extended rosette acquisition.

Four different volumes of time series were reconstructed from the functional study data acquired in experiment II.

1. The first volume of dynamic R_2^* maps was reconstructed applying the proposed R_2^* -and-field-map estimation method to the entire 88ms acquisition data ($\beta=1$, $\gamma=150$, $L=48$).
2. The second volume was chosen as the time series of the 24th subimage among the subimages, which were already reconstructed using the proposed spatio-

temporally regularized iterative reconstruction for the first volume.

3. The third volume was the time series of the static field-map-corrected T_2^* -weighted images using the fast iterative reconstruction [19]. At each time point, the image was reconstructed using the static field map estimated from the proposed R_2^* -and-field-map estimation method at the first time point. The reconstruction was done on the middle segment of the extended data, which started at 20ms from the beginning of the acquisition and ended at 62ms of the acquisition to match the effective echo time of the 24th subimage.
4. The fourth volume was the time series of the dynamic field-map-corrected T_2^* -weighted images using the fast iterative reconstruction. At each time point, the image was reconstructed using the dynamic field map estimated from the proposed R_2^* -and-field-map estimation method. The reconstruction was done on the same segment of the data as the third volume.

The NRMSE of the current iteration with respect to the previous iteration was used as the stopping criterion for the conjugate gradient iteration in the proposed methods. We stopped the iteration when the NRMSE of current iterate gets smaller than 10^{-4} . About 460 iterations were needed to reach that error level for the R_2^* -and-field-map estimation method. The number of iterations varied widely according to the choice of design parameters and the acquisition lengths.

3.4.2 Results

Figure 3.8 and figure 3.9 show the image reconstruction results from the first MRI experiment (Experiment I). Figure 3.8 shows all of the 24 subimages reconstructed using the proposed R_2^* -and-field-map-corrected reconstruction method. As was found in the simulation results, the later echo subimages had more artifact than those in

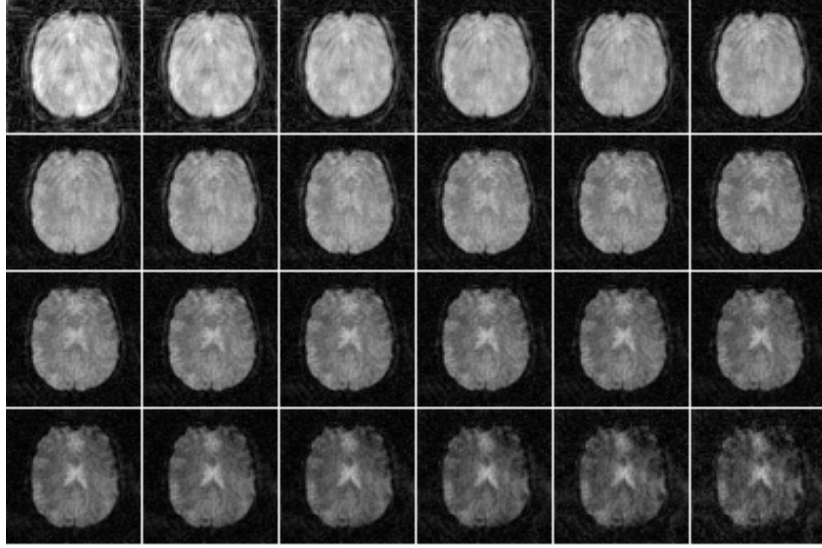


Figure 3.8: Experiment I : The 24 reconstructed subimages from a single shot gradient echo rosette data set (readout = 44.4ms). The left top image is the first subimage.

the middle. The streaking artifact present in the earlier echo subimages are due to imperfect fat presaturation, and to error in the initial field map. The subimages clearly show the temporal evolution of the R_2^* contrast between brain tissues and CSF in ventricles.

Figure 3.9 compares the standard field-map-corrected/uncorrected T_2^* -weighted image with that of the proposed R_2^* -and-field-map-corrected reconstruction method. The image from the proposed R_2^* -and-field-map-corrected reconstruction successfully recovered the signal in the high off-resonance area, where the image without field map correction lost most of the intensity (Figure 3.9 (a) and (c)). Figure 3.9 (b) shows the field-map-corrected T_2^* -weighted image with the initial field map estimated using the improved 'two-point' method in section 3.2.5.

The following figures show the results from the second functional MRI experiment (Experiment II). Figure 3.10 shows the R_2^* and field map of the 10th time point of

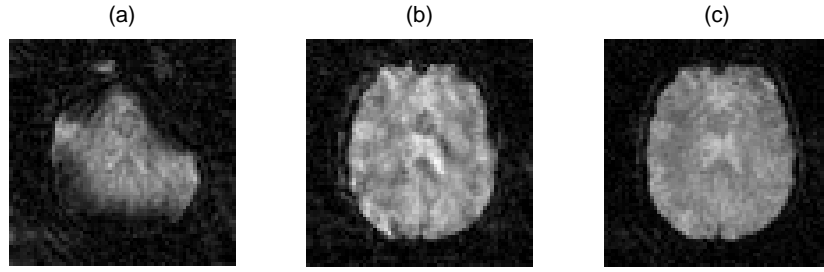


Figure 3.9: Experiment I : (a) Image without field map correction. (b) Field-map-corrected T_2^* -weighted image reconstructed from standard iterative reconstruction. (c) Proposed R_2^* -and-field-map-corrected reconstruction (12th subimage in Figure 3.8). In (b) and (c), the initial field map, which was estimated using the method described in section 3.2.5, was used in the reconstructions.

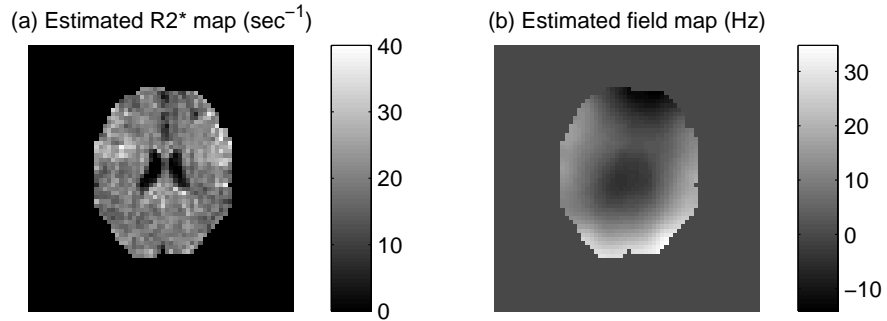


Figure 3.10: Experiment II : The estimated R_2^* map and field map from the proposed R_2^* -and-field-map estimation method.

the 7th slice estimated from the proposed R_2^* -and-field-map estimation method. The R_2^* map exhibits the anatomical structure of the brain, and the high field map area (bottom of the R_2^* map) shows no artifact from the field map error.

Figure 3.11 shows the results of four different reconstructions on the functional study data. The first row shows the activation map and the averaged time course of the dynamic R_2^* maps estimated using the proposed R_2^* -and-field-map-estimation method. The second row shows the activation map from the 24th subimages reconstructed using the proposed spatio-temporally iterative reconstruction method.

The third and fourth row show the results from the static and dynamic field-map-corrected T_2^* -weighted images using fast iterative reconstruction [19]. For each reconstruction, the numbers of the activated pixels were 16, 18, 20 and 23 pixels respectively.

Figure 3.12 (a) shows the normalized averaged time series of one slice in the functional study. We regressed out the reference waveform using linear least square fitting before averaging the time series over the entire brain region. Only the time series of static field-map-corrected T_2^* -weighted image exhibits the time varying trend of the field map during the functional study. Figure 3.12 (b) shows the average time course of the dynamic field map estimated using the proposed R_2^* -and-field-map-estimation method.

3.5 Discussion

Most of the error in the R_2^* estimates came from mismatch between the point spread functions (PSF) of subimages. We observed that the earlier images had enhancement in the edges of the simulation object, and the later subimages had smoother edges as shown in Figure 3.7. The error in the field map estimates was also concentrated around the edge of the simulation object. This result is the opposite to the results observed in [64], which used multi-spin echo radial data, and it is an interesting research problem to consider the effect of the spatio-temporal sampling scheme on the PSF of images. Preliminary data shows that this PSF mismatch could be reduced with well designed temporally varying γ values, and further investigation is required. Separate spatial regularization of the magnitude and phase of subimages [65] may also help to reduce the artifact.

Since there is no mono-exponential decay assumed in the reconstruction model,

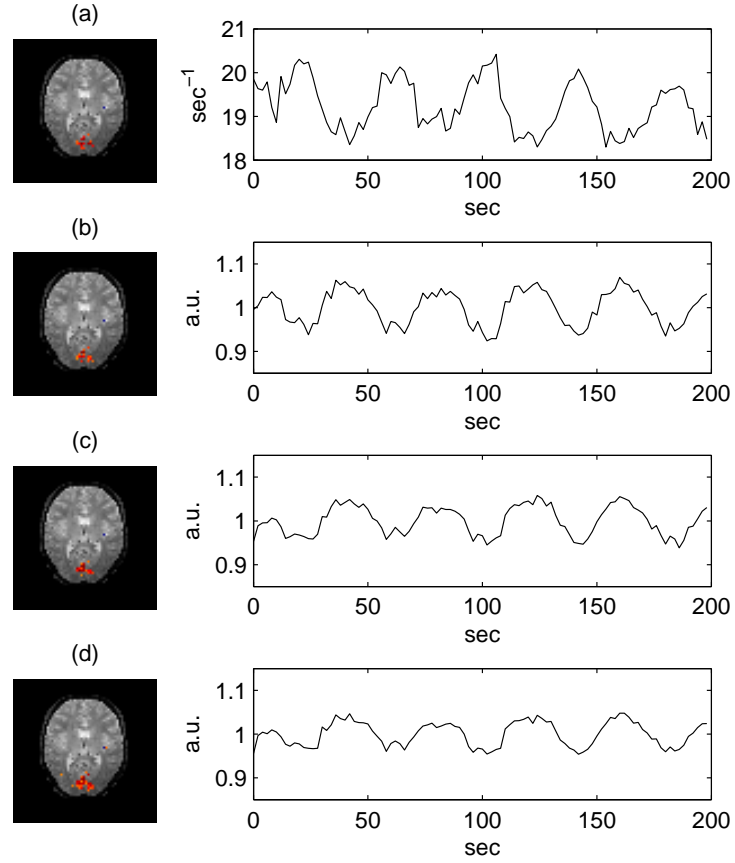


Figure 3.11: Experiment II : Activation maps (left) and the corresponding averaged time course of the activated pixels (right). (a) The dynamic R_2^* maps from the proposed R_2^* -and-field-map-estimation method. (b) The 24th subimages from the proposed R_2^* -and-field-map-estimation method. (c) The field-map-corrected T_2^* -weighted images with static field map estimated from the first time point. (d) The dynamic field-map-corrected T_2^* -weighted images, where dynamic field maps were estimated from the proposed R_2^* -and-field-map-estimation method.

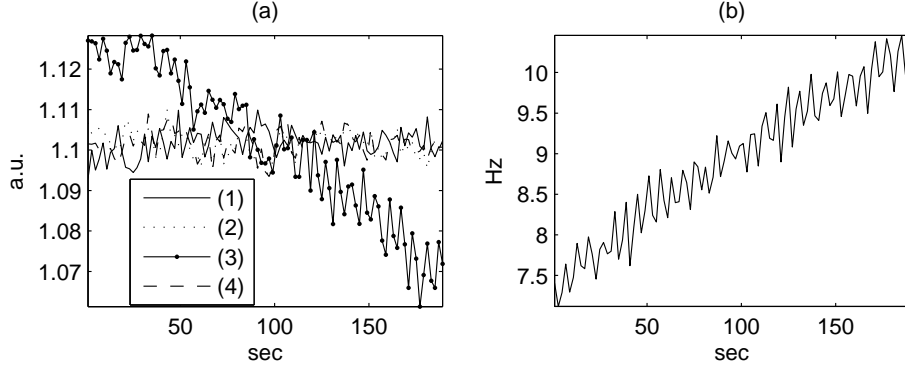


Figure 3.12: Experiment II : (a) The normalized mean time series of the four experiments from Fig. 3.11. Each line represents the time series of the R_2^* maps from the proposed R_2^* -and-field-map estimation method (1), the 24th subimages from the proposed R_2^* -and-field-map estimation method (2), the field-map-corrected T_2^* -weighted images using the field map estimated from the first time point (3), and the dynamic field-map-corrected T_2^* -weighted images using the field maps estimated from the proposed R_2^* -and-field-map-estimation method (4). (b) The average time course of the dynamic field map estimated using the proposed R_2^* -and-field-map-estimation method.

the subimages can also exhibit multi-exponential decays. Other preliminary results (not shown) indicate that the proposed scheme can reconstruct bi-exponential decays in the subimages. However, a robust nonlinear estimation algorithm is required to estimate the amplitudes and decay values from a single decay curve.

In this work, the parameters for the PR and rosette trajectories were not optimized. A random view ordering of PR provided less error in the R_2^* estimates than the sequential order. This can be explained by considering the sampling in 3D k-t space. The randomized view ordering provides more evenly distributed sampling in 3D than sequential ordering, therefore it allows better condition for the reconstruction scheme to estimate the missing points in the k-t space. However, randomized view ordering would require more scan time due to the increased transition time between spokes. The rosette trajectory can provide a pseudo-randomized view ordering without increased transition time between petals.

The proposed method can be easily extended to multi-shot methods and the par-

tially parallel imaging methods [41, 42] to speed up the acquisition or to improve the accuracy of estimates. In addition, dynamic imaging methods such as UNFOLD [40] use a series of undersampled trajectories to collect the data and applies a temporal low-pass filter to reduce the aliasing artifacts on each frame. The proposed method can be easily extended to reconstruct the unaliased images without specific temporal filters.

In the functional study, it was observed that the number of activated pixels was the smallest in the R_2^* mapping. One of the reasons could be the erroneous estimate of R_2^* maps due to the artifacts from the residual fat signal and the field map errors as shown in Figure 3.8. On the other side, the dynamic field-map-corrected images generated more activated pixels than the static field-map-corrected images in accordance with the results in [53].

The proposed R_2^* -and-field-map reconstruction method successfully reconstructed the R_2^* -and-field-map corrected image in the simulations. This indicates that the proposed method is robust to the R_2^* -and-field-map errors in the system model. The maximum allowable field map error can be calculated using the length of data segment as described in section 3.2.5. In addition, given the initial field map within the maximum allowable range of field map error, the proposed R_2^* -and-field-map estimation method was able to provide not only the dynamic field maps but also dynamic field-map-corrected subimages. The method requires an initial guess of the static (or dynamic if possible) field map, but it is obvious that the method is able to produce dynamic information of the field map change as it was presented in the functional study results.

The proposed spatio-temporally regularized iterative reconstruction is not limited to single-shot PR or rosette trajectories. As long as a trajectory acquires the center

of k-space multiple times during the acquisition, the reconstruction method can be applied to reconstruct the temporal change of the imaging object. The frequency and the number of the sampling of DC will determine the spectral FOV and the resolution for the reconstruction of dynamic change of the object. A series of quick spiral out-in/in-out trajectories, multiple undersampled EPI trajectories, or single-shot propeller imaging are conceivable choices. Further investigation is required to study the benefit of using such trajectories and also to determine the optimal trajectories given *a priori* information on the dynamics of the imaging object.

The biggest concern of the proposed method is the reconstruction speed. A new faster iterative reconstruction method such as [66] could help to reduce the reconstruction time significantly. A well designed preconditioner [23] and good initial guess of subimages will also help to reduce the reconstruction time.

3.6 Conclusion

We have proposed a spatio-temporally regularized iterative reconstruction method to reconstruct R_2^* -and-field-map-corrected images and to estimate dynamic R_2^* and field maps. The proposed method required no *a priori* knowledge of R_2^* map, but only pre-estimated low accuracy field map was required. Through simulations and functional experiments, we verified that the method is capable of the accurately reconstructing the R_2^* -and-field-map-corrected images and estimating the dynamic R_2^* and field maps.

CHAPTER IV

2D k-space trajectory measurement

4.1 Introduction

In fast MR imaging, high gradient slew rates are often required, which can lead to distortions in the gradient waveforms due to the eddy currents. Fast imaging methods such as spiral and echo-planar imaging (EPI) suffer from artifacts caused by such gradient distortions [67–69].

One approach to reduce the distortion of gradient waveforms is hardware pre-compensation. However, hardware pre-compensation is not enough for some MR applications such as spiral in-out imaging [70, 71], and the eddy current effects having short time constants ($\ll 1\text{ms}$) are often difficult to eliminate using such pre-compensation techniques [68].

Another approach is to measure the actual k-space trajectory, and use the measured information in post processing. Many k-space trajectory measurement methods have been introduced. Several methods used extra encoding gradients [72–74] to measure 2D or 3D k-space trajectories, but an extensive number of encoding steps can lead to excessive scan time. Another method by Mason et al. [75] used a small sphere to estimate the k-space trajectories from the phase of the received signal. This approach required an extra surface coil to have adequate Signal to Noise Ratio

(SNR), and the accuracy was limited by the spatial resolution of the gradient echo image, which was used to determine the location of the sphere. Another by Duyn et al. [69] used a slab excitation instead of using a small object. It did not require extra surface coil, nor estimation of the location of a sample, but it was limited to measuring only one channel at a time. Goodyear et al. [76] proposed to use a uniform phantom with short T_2 and T_2^* to measure instantaneous phase of the data with multiple adjacent RF excitations.

In this chapter, we propose a new technique that uses the MR signal from a pencil-shaped excitation volume. The proposed method has several advantages: it does not require a surface coil or a point phantom, it can be implemented with only a small modification to the pulse sequence, it only requires eight measurements when signal averaging is not necessary, it can measure B_0 fluctuation due to B_0 eddy currents while fully compensating for field inhomogeneity, it can determine the effects of gradient cross coupling between two channels.

A phantom experiment was performed to measure spiral in-out trajectory [77] and B_0 fluctuation. A comparison between the measured trajectory and the designed trajectory was done via the reconstruction of a human scan data. In addition, a simulation study was performed to investigate the effect of the trajectory distortion and the B_0 fluctuation on image reconstruction.

4.2 Methods

4.2.1 Theory

The proposed measurement method consists of measuring the MR signal from four different spatial locations.

First, to measure the k-space trajectory of the X channel, the *pencil excitation* is

applied at $(X_0, 0)$. The *pencil excitation* is composed of a slice selective 90 degree pulse in X at X_0 , and followed by an 180 degree pulse in Y at 0 (Figure 4.1 (a)). After the pencil excitation pulse, the target readout gradients (both channels) are played while the data $S_{\text{on}}(t; X_0, 0)$ is collected (Figure 4.1 (b)). Assuming the slice thickness is small enough, the received signal is

$$(4.1) S_{\text{on}}(t; X_0, 0) \approx e^{-i2\pi(k_x(t)X_0)} e^{-i \int_0^t \gamma b_0(\tau) d\tau} \int_{-\Delta z/2}^{\Delta z/2} M(X_0, 0, z) e^{-i\omega(X_0, 0, z)t} dz,$$

where γ is the gyromagnetic ratio; Δz is the length of the excited pencil-shaped volume in z axis; $M(X_0, 0, z)$ is the transverse magnetization in the excited volume; ω is the spatially varying but time invariant off-resonance; and $\gamma b_0(\tau)$ is the spatially invariant main field fluctuation caused by the B_0 eddy current. To cancel out any unrelated eddy current effect and field inhomogeneity, we also acquire $S_{\text{off}}(t; X_0, 0)$ while the target readout gradients are not played. Figure 4.1 (b) illustrates the pulse sequences with/without the target gradients.

Second, to account for B_0 fluctuations, we acquire another pair of data sets at the opposite location of the axis, i.e., $(-X_0, 0)$. From the four measurements, we estimate the k-space trajectory of the target channel, $k_x(t)$, using the following:

$$(4.2) \quad \hat{k}_x(t) = -\frac{1}{4\pi X_0} \mathfrak{U} \left(\angle \left(\frac{S_{\text{on}}(t; X_0, 0) S_{\text{off}}(t; -X_0, 0)}{S_{\text{off}}(t; X_0, 0) S_{\text{on}}(t; -X_0, 0)} \right) \right),$$

where $\mathfrak{U}(\cdot)$ denotes 1D phase unwrapping operation.

The phase accumulation from B_0 fluctuation $\phi_0(t) = \int_0^t \gamma b_0(\tau) d\tau$, or B_0 term, is estimated from the same measurement using

$$(4.3) \quad \hat{\phi}_0(t) = -\frac{1}{2} \mathfrak{U} \left(\angle \left(\frac{S_{\text{on}}(t; X_0, 0) S_{\text{on}}(t; -X_0, 0)}{S_{\text{off}}(t; X_0, 0) S_{\text{off}}(t; -X_0, 0)} \right) \right).$$

Similarly, the k-space trajectory of the other target channel, $k_y(t)$, is estimated from the measurements at $(0, Y_0)$, and $(0, -Y_0)$ with/without the target readout

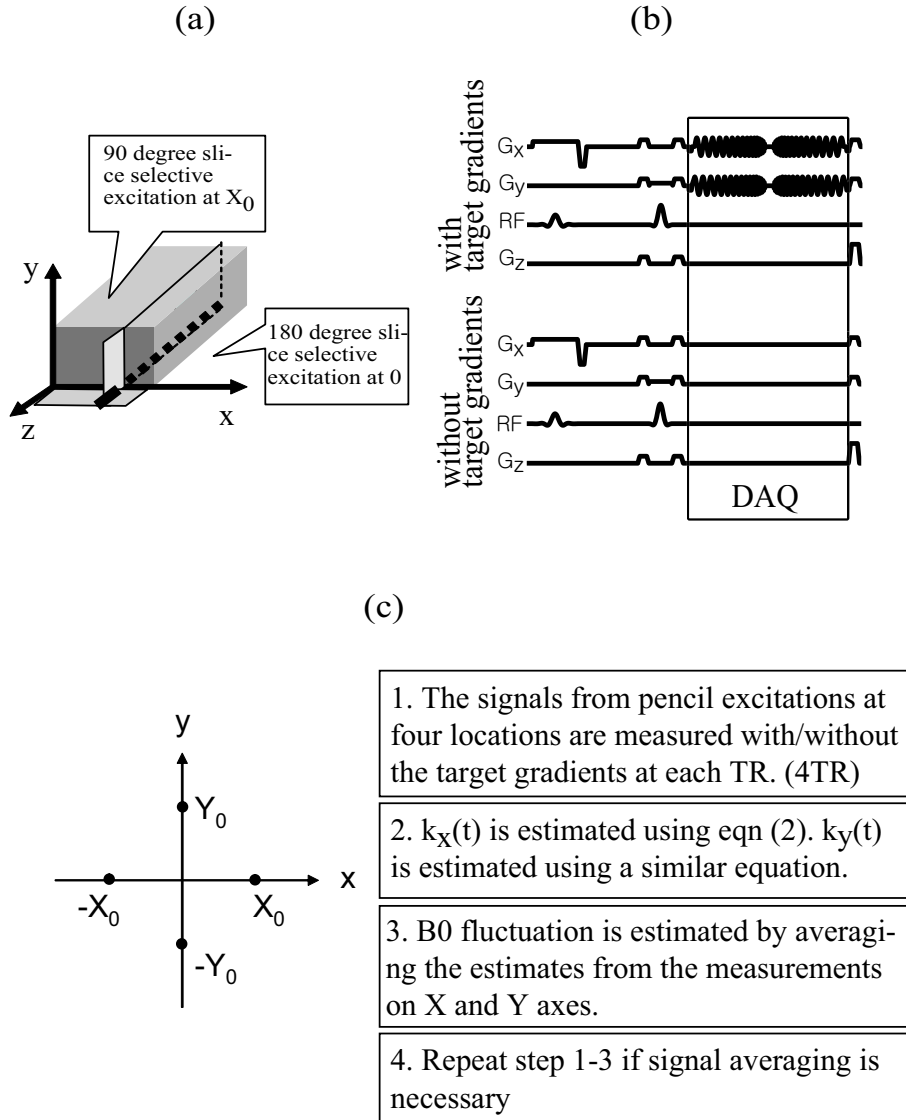


Figure 4.1: (a) Illustration of a pencil excitation at $(X_0, 0)$. (b) The pulse sequence used to measure $k_x(t)$. (c) The proposed k-space trajectory measurement scheme

gradients. The B_0 term is estimated from these measurements, and averaged with the $\phi_0(t)$ estimated from the X channel measurements to get the final estimated $\phi_0(t)$. Figure 4.1 (c) summarizes the complete procedure of the proposed k-space trajectory measurement scheme.

4.2.2 Experiments

All experiments were done in GE 3T scanner (EXCITE 2.0, GE Healthcare, Waukesha, WI). The vendor-provided eddy current pre-compensation was turned on during all experiments.

A spiral in-out trajectory was used in the trajectory measurement and for imaging. The maximum gradient slew rate was 18 G/cm/ms, and the maximum gradient amplitude was 2.6 G/cm. The time gap between spiral in and spiral out trajectories was 1.1 ms, and the total readout was 36.5 ms. The receiver bandwidth was 250 kHz (sampling time $4\mu\text{s}$). Both the spiral in (first half) and spiral out (second half) trajectories were designed to provide spatial resolution of 3.75 mm and a 24 cm FOV.

Phantom experiment

A spherical phantom (NiCl_2 solution, 17 cm diameter) was used in the phantom experiment. The cross sectional area of the pencil excitation was chosen to be 3 mm by 3 mm to have enough volume for high SNR, while preventing the k-space coverage of the trajectory from reaching the first zero of the spectrum of the excited volume. The locations in the measuring plane (X-Y) were ± 5 cm from the isocenter of the gradient system on each axis. TR was 2 s and the echo time was 50 ms, where the echo time was defined as the time difference between the center of the 90 degree pulse and the center of the readout. To reduce the scan time to 4TRs, the measurements on each axis were interleaved, and the amplitudes of the spoiler gradients were increased at each measurement to reduce the stimulated echo. Using

the equations in the previous section, $k_x(t)$, $k_y(t)$ and $\phi_0(t)$ were estimated from the measured data sets. No data averaging was necessary.

In addition, the k-space measurement was repeated without playing the spiral in-out gradient in the X channel. By this experiment, we were able to measure the cross coupling of gradient channels in the estimated $k_x(t)$.

Human experiment

One human subject was scanned in the GE 3T scanner. Written informed consent was obtained from a subject prior to the MRI scan as approved by the University of Michigan Institutional Review Board. Gradient echo images from two axial slice locations were obtained using the identical spiral in-out trajectory used in the k-space measurement sequence. TR was 2 s, and TE was 25 ms. Images were reconstructed using the designed trajectory and then using the measured trajectory via fast iterative reconstruction with field map correction [19].

Effect on the reconstruction

A k-space data set was generated from a 64 by 64 discrete object and a simulated off-resonance map (min: -54 Hz, max: 5 Hz) using the estimated k-space trajectory and the B_0 term from the phantom measurements. For the simulations, we first low-pass filtered the B_0 term, $\phi_0(t)$, and removed any linear trend.

Four images were reconstructed from the simulated k-space data using 1) the measured trajectory and the measured $\phi_0(t)$ (the reference reconstruction), 2) the designed trajectory with $\phi_0(t)$, 3) the measured trajectory without $\phi_0(t)$, and 4) the designed trajectory without $\phi_0(t)$. We used a fast iterative reconstruction method [19] with a slight modification to include the time-varying B_0 fluctuations in the reconstruction system model. The NRMSE (Normalized Root Mean Squared Error) of the magnitudes of the reconstructed images (2,3,4) was measured with respect to

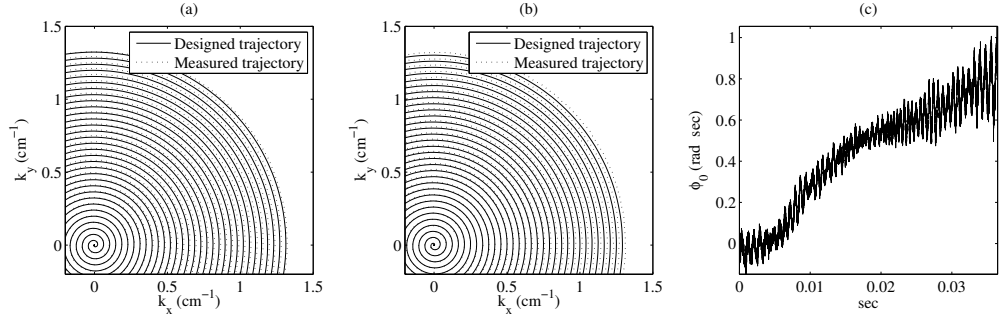


Figure 4.2: (a) The measured trajectory and the designed trajectory for the first half (spiral in) of the spiral in-out trajectory (b) The measured trajectory and the designed trajectory for the second half (spiral out) of the spiral in-out trajectory (c) The measured phase accumulation from B_0 fluctuation, $\phi_0(t)$.

the magnitude of the reference reconstruction.

4.3 Results

Figure 4.2 shows the measured k-space trajectory and the designed trajectory on 2D k-space, along with the estimated B_0 term, $\phi_0(t)$. At this coarse scale, the measured k-space trajectory is not noisy, and it deviates slightly from the designed trajectory. Note that the deviation is larger in the higher spatial frequency region of the k-space, where more trajectory error is accumulated. The RMSD (Root Mean Squared Difference) of the measured trajectory with respect to the designed trajectory were 0.0215 cm^{-1} and 0.0188 cm^{-1} for the X and Y channels respectively. Since the self-induced eddy current term often manifests as gradient delay, we measured the delay of the measured trajectory and the designed trajectory. The cross correlation was done on the ten times oversampled trajectory waveforms. The delays were measured for both spiral in and spiral out on each channel. Table 4.1 shows the measured delays.

Figure 4.3 shows the measured cross term in the X channel. Since there was no gradient waveform played in the X channel during this measurement, the waveform,

$k_x(t)$		$k_y(t)$	
spiral in	spiral out	spiral in	spiral out
0.7 samples	0.3 samples	0.9 samples	0.5 samples

Table 4.1: Delays of the measured trajectory with respect to the designed trajectory ($4 \mu\text{s}$ sampling time)

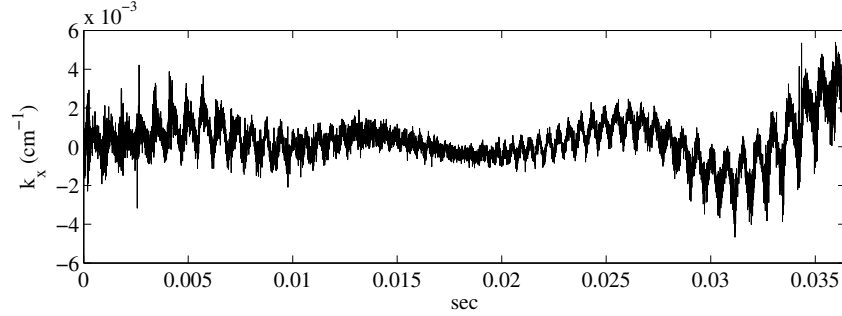


Figure 4.3: The cross coupling of the gradient channels was measured by setting the amplitude of the X readout gradient as 0, and measuring $k_x(t)$ while the other channel was on using the proposed measurement method.

$k_x(t)$, shown in the figure reveals the cross term induced by $k_y(t)$.

The human scan data was reconstructed with field map correction using the measured trajectory and the designed trajectory. Figure 4.4 shows that using the measured trajectory resulted in less artifacts in the reconstructed images.

The simulation results are shown in figure 4.5 to demonstrate the effect of the trajectory distortion and the B_0 fluctuation on image reconstruction. Most of the reconstruction error of the magnitude images is due to the difference between the measured trajectory and the designed trajectory. Figures 4.5 (b) and (d) indicate that using the designed trajectory in the reconstruction caused a blurring in the images. The effects of the B_0 fluctuations on the magnitude images were minimal. However, without $B_0(t)$ correction, the reconstructed images had a global shift in the phase.

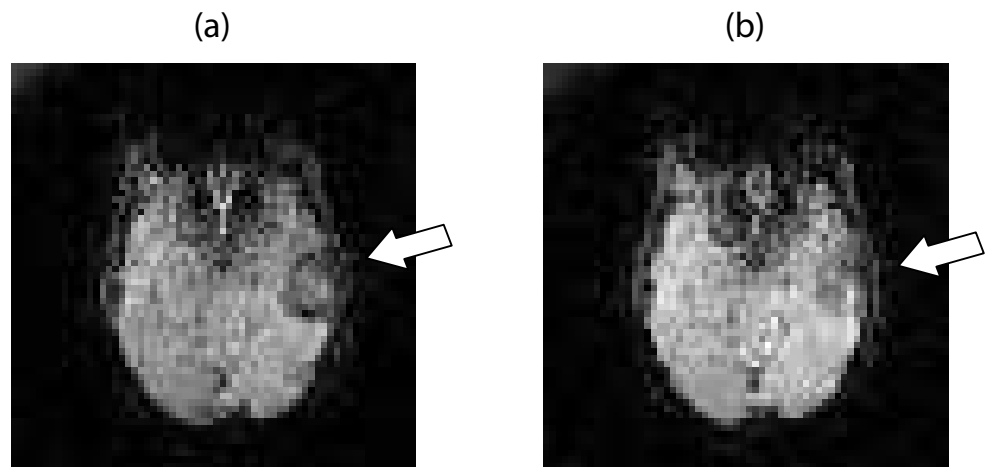


Figure 4.4: The images reconstructed from spiral in-out data in the human experiment. (a) The designed k-space trajectory was used for the reconstruction. (b) The measured trajectory was used for the reconstruction. The arrows indicate reduction of the reconstruction artifacts when the measured trajectory was used.

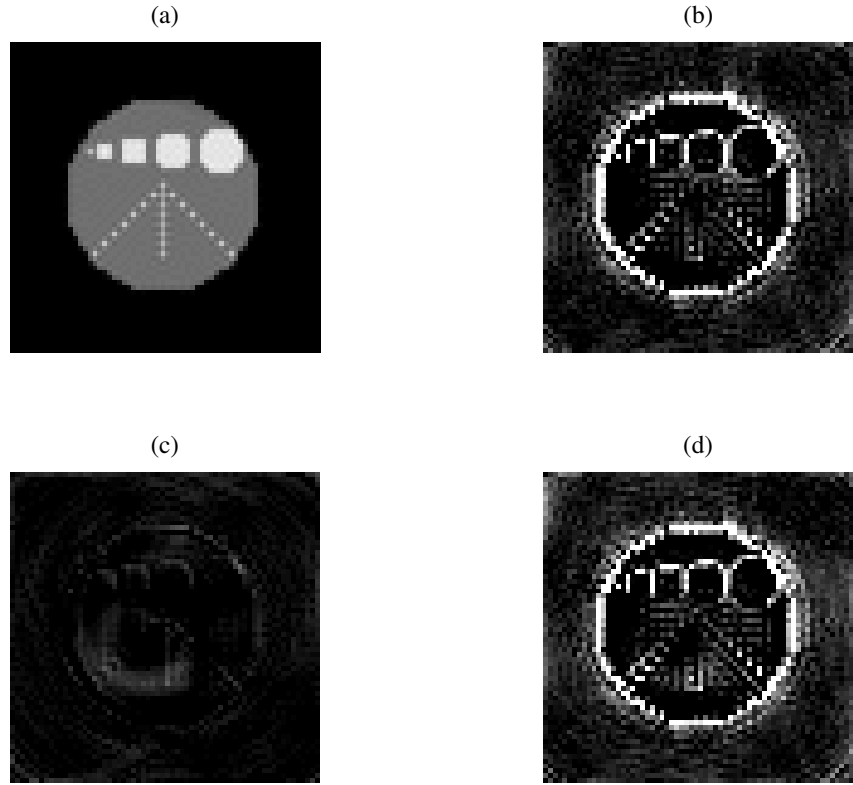


Figure 4.5: Simulation results using the measured k-space trajectory and B_0 fluctuation. The k-space data was synthesized using the measured k-space trajectory and $\phi_0(t)$, then reconstruction was done by incorporating the following variations into the reconstruction system model. (a) The reference reconstruction : The measured k-space trajectory and $\phi_0(t)$, (b) Difference map between the reference reconstruction and the magnitude image using the designed k-space trajectory with $\phi_0(t)$ (NRMSE=0.0534), (c) Difference map between the reference reconstruction and the magnitude image using the measured k-space trajectory without $\phi_0(t)$ (NRMSE=0.0114), (d) Difference map between the reference reconstruction and the magnitude image using the designed k-space trajectory without $\phi_0(t)$ (NRMSE=0.0534). All difference maps were scaled by 22 for visualization purpose. The NRMSE were measured with respect to the reference reconstruction (a) inside of the object.

4.4 Discussions and Conclusions

We have demonstrated that the proposed method can be used to measure 2D k-space trajectories using a pencil excitation. The method is able to capture the cross-coupling of gradient channels. Together with the self-induced eddy current term, the cross-coupling caused the actual k-space trajectory to deviate slightly from the designed trajectory even with the vendor-supplied eddy current compensation enabled.

The self-induced eddy current often manifests itself as a delay in the gradient waveform as well as distortions in the waveforms. The delay, along with the delay between the gradient amplifier and the data acquisition unit, can be easily fixed in the pulse sequence program by including a timing delay in the data acquisition window. In spiral trajectories, a mismatch in delay can be observed as a slight rotation in the reconstructed images. One could determine the delay by trial and error from such rotations, but its accuracy is limited. In addition, the eddy current related delay varies throughout the readout in accordance with the first derivative of the gradient waveform. Therefore, measuring spiral k-space trajectory is desirable to improve the reconstruction accuracy. For rosette trajectories, the artifact from delay mismatch manifests as image intensity loss. A simple integration of image intensity can be used as a measure to determine the right delay.

The proposed method was also able to measure B_0 fluctuations that can lead to additional error in the image reconstruction if uncorrected. The time derivative of the estimated (and denoised) $\phi_0(t)$ reveals that the magnitude of the instantaneous off-resonance can reach up to 100Hz. However, this instantaneous change does not lead to significant accumulation of the phase in the received signal, therefore it had

minimal effect on the image reconstruction.

The accuracy of the proposed method is dictated by the accuracy of the pencil excitation. Any nonlinearity in the gradient B field would cause unwanted scaling of the measured trajectories. In addition, the spatial gradient of the B_0 field inhomogeneity in the excited volume would cause distortions in the local k-space trajectories and result in lower SNR in the measurement.

The proposed method requires relatively small scan time (4TRs) and small modifications to the pulse sequence, and there was no need for dedicated equipment. One could reduce the scan time further to 2TRs by interleaving all measurements and also integrate the measuring sequence into the regular prescan procedure. One could also measure the k-space trajectories with the subject instead of a spherical phantom. However, our preliminary data shows that even with the TR of 5s, and 20 times averaging, the SNR is too low due to the complex structure of the off-resonance in the brain and the contamination by physiological noise and blood flow.

Based on the principle of the proposed 2D method, an easy extension to measuring 3D k-space trajectories is conceivable. However, signal averaging would be necessary as the excitation volume is reduced to a small 3D cube.

CHAPTER V

Conclusions and future work

5.1 Conclusion

The principal objective of this work was to develop a better reconstruction method for SMART imaging. SMART method had been shown to be a fast and effective way of functional imaging. But, the previously proposed reconstruction method by Noll et al. [2] suffered from the artifacts from the off-resonance slices. We proposed a physics model based iterative reconstruction method (iSMART) to reduce these artifacts. In our simulation, the proposed method was shown to reduce the reconstruction error by about 70% from that of the conjugate phase reconstruction (CPSMART). It was also found that the spatial resolution was slightly reduced in iSMART reconstruction. In the functional study, iSMART resulted more activated pixels than CPSMART in most of the slices, but further investigation is required to draw a conclusion whether one method is better than the other in terms of functional detectability.

The proposed iterative reconstruction was more sensitive to the error in the field map than CP reconstruction. Therefore a very accurate field map estimation procedure was required. An improvement on the initial field map was done by applying the spatio-temporally regularized reconstruction described in chapter III. A greater number of shots for the field map estimation could be used for more accurate es-

timation of the field map, but longer scan time would lower the accuracy of the field map due to the field map change during the extended data acquisition. The spatio-temporally regularized reconstruction provided a robust reconstruction of the field-map corrected image even when inaccurate field map was used in the system model. The robust reconstruction can be useful, when the vendor-provided shimming is not sufficient and when a long acquisition for field map estimation is not desirable. We also estimated a field map with better accuracy, and R_2^* map without prior information by extending the acquisition.

The accuracy of the system model of the iterative reconstruction can be improved further by measuring the k-space trajectory. The proposed pencil excitation allowed us to measure the 2D k-space trajectory at the same time, therefore, the cross talk between two channels can be measured. From the same data set, we measured the fluctuation of the main magnetic field due to the B_0 eddy current. The method does not require extra equipment such as a point phantom or a surface coil. Our result showed that the difference between the measured trajectory and the designed trajectory was mostly manifested as a group delay of the gradient waveform. In rosette trajectory, the delay can be detected more efficiently than spiral trajectories.

The measurement of k-space trajectory does not have significant impact on the image reconstruction error. Therefore, in our iSMART experiments, the k-space measurement was not performed. With the use of other scanners with different gradient system, the trajectory error could have more significant impact on the image reconstruction.

In the following list, we state the contribution of this thesis to the field of MRI.

1. We developed a new iterative reconstruction method for SMART acquisition (iSMART), and implemented SMART method in a 3T scanner for the first time.

The proposed reconstruction method reduced the artifacts from off-resonance slices, which can be found in the conventional CP reconstruction. It also resulted more activated pixels in most slices, higher time-series SNR, but slightly lower in-plane spatial resolution.

2. We developed a new robust R_2^* -and-field-map corrected image reconstruction method based on the spatio-temporal regularization. The formulation of temporally segmented system matrix was not done in MR research field previously. It allows a robust R_2^* -and-field-map corrected image reconstruction when an inaccurate field map and no R_2^* map are provided in the system model.
3. Based on the robust R_2^* -and-field-map corrected image reconstruction, we also developed a novel dynamic R_2^* and field mapping method for functional MRI. The dynamic field map estimation revealed the field map fluctuation during a functional study, and a functional activation was detected by the dynamic R_2^* maps.
4. We developed a new 2D k-space trajectory measurement method, which can quickly measure the k-space trajectory as well as the crosstalk between two channels and the B_0 fluctuation.

5.2 Future work

Acceleration of iterative methods by preconditioning

The proposed iterative methods for rosette trajectory are slower than other non-iterative or iterative reconstruction for conventional single slice imaging. In the context of numerical linear algebra, the use of preconditioner is a common way to accelerate the inverse problem of $Y = AX$ [23]. The idea of preconditioning is to pre-multiply a matrix M to the system matrix A to make the eigenvalues of MA to be

clustered. A good preconditioner should be easily computed, and the multiplication of it to a vector should be done quickly. A reasonable preconditioner would be an approximation to the inverse of the system matrix, or the minimizer of $\|I - MA\|$. For a Toeplitz system matrix, circulant preconditioners are popular choices, since the matrix-vector multiplication can be done using FFT. Several ways of constructing circulant preconditioners are found in [78].

The hessian matrices of the proposed iterative methods are either Toeplitz (spatio-temporally regularized iterative reconstruction, when field map is not included in each subsystem), or composed of block matrices which are weighted linear sum of Toeplitz matrices (iSMART). Further investigation will be necessary to find a circulant preconditioner for a linear sum of Toeplitz block matrices.

Acceleration of iterative methods by Toeplitz based iterative reconstruction

Toeplitz-based iterative reconstruction [66] is a faster method than the NUFFT-based iterative reconstruction [19]. The Toeplitz-based method is faster than NUFFT, because it does not require the interpolations in k-space. In [66], the Toeplitz-based iterative reconstruction was found to be about 2 times faster than the NUFFT-based iterative reconstruction. This method can be readily applied to the proposed iterative methods for extra speed-ups.

Investigation of other trajectories for spatio-temporally regularized iterative reconstruction

The proposed spatio-temporally regularized iterative reconstruction is not only limited to rosette trajectories or single-shot PR trajectories. It can be applied to any trajectory that resamples the origin of k-space multiple times. The current formulation has limitation that each segment should include samples near the origin to

provide meaningful subimages. Therefore, multi-echo interleaved spiral in-out/out-in trajectories, multi-echo interleaved EPI, or single shot propeller trajectories could be alternative choices. Since these trajectories would result in different undersampling artifacts, and the k-space coverage at each segment can be controlled in more intuitively than rosette, further investigation would result in very interesting research problems.

Combining with parallel imaging technique

SENSE (SENSitivity Encoding) was proposed by Pruessmann et al. [41] in 1999 as a parallel imaging technique. This method is used to speed up the acquisition several times using the coil sensitivity as extra information. Its application to non-Cartesian k-space trajectory was also tested and validated in [79]. The combination of SENSE and SMART will be a very attractive way to accelerate the brain volume imaging. Shorter rosette acquisition will result in wider spectral passband, then the off-resonance frequency between slices will have to be increased. A more accurate measurement of sensitivity map will be required, since the number of sensitivity map will be increased by the number of simultaneously excited slices. In case the accuracy of measured sensitivity maps are not sufficient, other parallel image reconstruction methods such as GRAPPA [47–49] can be considered.

Combining arterial spin labeling and SMART

Arterial Spin Labeling (ASL) method is an endogenous contrast perfusion imaging method in functional MRI. In this method, the spins at the arterial site are magnetically *tagged*, and the perfusion at the imaging site is measured from the difference between the *control* image and the *tagged* image [80]. Although this method provides better localization of neuronal activity and is less sensitive to subject motion, it suffers from low spatial and temporal resolution. A typical ASL implementation

acquires five to eight slices with a TR of $2 \sim 3$ s. Note that the actual temporal resolution of perfusion images is doubled as both control and tag images should be acquired. To increase the acquisition rate or number of slices, parallel imaging technique has been used with ASL [81]. In combination with parallel imaging method, or by itself, SMART can serve as a way to increase the number of imaging slices without loss of temporal resolution in ASL.

Comparison between the proposed dynamic R_2^* mapping and the conventional multi-echo method

In [8], the multiple gradient echo method was used to enhance the functional detectability in BOLD. The temporal/spatial SNR of the multi-echo method and the proposed dynamic R_2^* mapping can be done to investigate the effect of spatio-temporal regularization in the image reconstruction.

BIBLIOGRAPHY

BIBLIOGRAPHY

- [1] J. P. Wansapura, S. K. Holland, R. S. Dunn, and Jr. W. S. Ball. NMR relaxation times in the human brain at 3.0 tesla. *Journal of Magnetic Resonance Imaging*, 9:531–538, 1999.
- [2] D. C. Noll, S. J. Peltier, and F. E. Boada. Simultaneous multislice acquisition using rosette trajectories (SMART): A new imaging method for functional MRI. *Magnetic Resonance in Medicine*, 39:709–716, 1998.
- [3] R. L. Savoy, P. A. Bandettini, K. M. O’Craven, K. K. Kwong, T. L. Davis, J. R. Baker, R. M. Weisskoff, and B. R. Rosen. Pushing the temporal resolution of fMRI: Studies of very brief visual stimuli, onset variability and asynchrony, and stimulus-correlated changes in noise. In *Soc. of Magn. Reson. 3rd Scientific Meeting*, page 450, 1995.
- [4] D. G. Nishimura. Principles of magnetic resonance imaging. Department of Electrical Engineering: Stanford University, 1996.
- [5] S. Ogawa, T.M. Lee, A.S. Nayak, and P. Glynn. Oxygenation-sensitive contrast in magnetic resonance image of rodent brain at high magnetic fields. *Magnetic Resonance in Medicine*, 14:68–78, 1990.
- [6] P. A. Bandettini, E. C. Wong, R. S. Hinks, R. S. Tikofsky, and J. S. Hyde. Time course EPI of human brain function during task activation. *Magnetic Resonance in Medicine*, 25:390–397, 1992.
- [7] J.W. Belliveau, D.N. Jr. Kennedy, R.C. McKinstry, B.R. Buchbinder, R.M. Weisskoff, M.S. Cohen, J.M. Vevea, T.J. Brady, and B.R. Rosen. Functional mapping of the human visual cortex by magnetic resonance imaging. *Science*, 254:716–719, 1991.
- [8] S. Posse, S. Wiese, D. Gembris, K. Mathiak, C. Kessler, M.-L. Grosse-Ruyken, B. Elghahwagi, T. Richards, S. R. Dager, and V. G. Kiselev. Enhancement of BOLD-contrast sensitivity by single-shot multi-echo functional MR imaging. *Magnetic Resonance in Medicine*, 42:87–97, 1999.
- [9] S. Clare, S. Francis, P. G. Morris, and R. Bowtell. Single-shot T2* measurement to establish optimum echo time for fmri: Studies of the visual, motor, and auditory cortices at 3.0T. *Magnetic Resonance in Medicine*, 45:930–933, 2001.
- [10] R. S. Likes. Moving gradient zeugmatography. U.S. Patent 4,307,343, 1981.
- [11] D. C. Noll, S. J. Peltier, and F. E. Boada. Multishot rosette trajectories for spectrally selective MR imaging. 16:372–377, 1997.
- [12] W.T. Dixon. Simple proton spectroscopic imaging. *Radiology*, 153:189–194, 1984.
- [13] G. H. Glover and E. Schneider. Three-point Dixon technique for true water/fat decomposition with B_0 inhomogeneity correction. *Magnetic Resonance in Medicine*, 18:371–383, 1991.

- [14] J. I. Jackson, C. H. Meyer, D. G. Nishimura, and A. Macovski. Selection of a convolution function for fourier inversion using gridding. *IEEE Transactions on Medical Imaging*, 10(3):473–478, 1991.
- [15] J. O’Sullivan. A fast sinc function gridding algorithm for Fourier inversion in computer tomography. 4:200–207, 1985.
- [16] D. C. Noll, C. H. Meyer, J. M. Pauly, D. G. Nishimura, and A. Macovski. A homogeneity correction method for magnetic resonance imaging with time-varying gradients. *IEEE Transactions on Medical Imaging*, 10(4):629–637, 1991.
- [17] H. Schomberg. Off-resonance correction of MR images. *IEEE Transactions on Medical Imaging*, 18(6):481–495, 1999.
- [18] L.-C. Man, J. M. Pauly, and A. Macovski. Multifrequency interpolation for fast off-resonance correction. *Magnetic Resonance in Medicine*, 37:785–792, 1997.
- [19] B. Sutton, D. Noll, and J. Fessler. Fast, iterative image reconstruction for MRI in the presence of field inhomogeneities. *IEEE Transactions on Medical Imaging*, 22:178–188, feb 2003.
- [20] J. D. O’Sullivan. Fast sinc function gridding algorithm for fourier inversion in computer tomography. *IEEE Transactions on Medical Imaging*, 4, 1985.
- [21] A. Dutt and V. Rokhlin. Fast fourier transforms for nonequispaced data. *SIAM Journal on Scientific Computing*, 14(6):1368–1393, 1993.
- [22] G. H. Golub and C. F. Van Loan. *Matrix Computations*. The Johns Hopkins University Press, Baltimore, third edition, 1996.
- [23] L. N. Trefethen and III D. Bau. *Numerical Linear Algebra*. SIAM, 1997.
- [24] J. A. Fessler and W. L. Rogers. Spatial resolution properties of penalized-likelihood image reconstruction: space-invariant tomographs. *IEEE Transactions on Image Processing*, 5:1346–1358, 1996.
- [25] M. Soumekh. Reconstruction and sampling constraints for spiral data. *IEEE Trans. Acoustics, Speech, Signal Processing*, 37:882–891, 1989.
- [26] C. J. Hardy, H. E. Cline, and P. A. Bottomly. Correcting for nonuniform k-space sampling in two-dimensional NMR selective excitation. *J. Magn. Reson.*, 87:639–645, 1990.
- [27] R. D. Hoge, R. K. S. Kwan, and G. B. Pike. Density compensation functions for spiral MRI. *Magnetic Resonance in Medicine*, 38:117–128, 1997.
- [28] A. M. Takahashi. Consideration for using the Voronoi areas as a k-space weighting function. In *ISMRM Eighth Scientific Meeting*, page 92, 1999.
- [29] J. G. Pipe and P. Menon. Sampling density compensation in MRI: Rationale and an iterative numerical solution. *Magnetic Resonance in Medicine*, 41:179–186, 1999.
- [30] Daniel Rosenfeld. An optimal and efficient new gridding algorithm using singular value decomposition. *Magnetic Resonance in Medicine*, 40:14–23, 1998.
- [31] H. Sedarat and D. G. Nishimura. On the optimality of the gridding reconstruction algorithm. *IEEE Transactions on Medical Imaging*, 19(4):306–317, 2000.
- [32] J. A. Fessler and B. P. Sutton. Nonuniform fast fourier transforms using min-max interpolation. *IEEE Transactions on Signal Processing*, 51(2), 2003.
- [33] N. Nguyen and Q. H. Liu. The regular fourier matrices and nonuniform fast fourier transforms. *SIAM Journal on Scientific Computing*, 21(1):283–293, 1999.

- [34] L. Greengard and J. Lee. Accelerating the nonuniform fast Fourier transform. *SIAM review*, 46(3):443–454, 2004.
- [35] J.D. Bourland, J.A. Nyenhuis, and D.J. Schaefer. Physiologic effects of intense MRI gradient fields. *Neuroimaging Clin North Am*, 9:363–377, 1999.
- [36] R.A. Jones, O. Haraldseth, T.B. Mueller, P.A. Rinck, and A.N. Oksendal. k-space substitution: A novel dynamic imaging technique. *Magnetic Resonance in Medicine*, 29:830–834, 1993.
- [37] J.J. Van Vaals, M.E. Brummer, W.T. Dixon, J.J. Tuithof, J. Engels, R.C. Nelson B.M. Gerety, J.L. Chezmar, and J. A. den Boer. Keyhole method for accelerating imaging of contrast agent uptake. *Journal of Magnetic Resonance Imaging*, 3:671–675, 1993.
- [38] Z.P. Liang and P.C. Lauterbur. An efficient method for dynamic magnetic resonance imaging. 13:677–686, 1994.
- [39] J. Tsao, P. Boesiger, and K.P. Pruessmann. k-t BLAST and k-t SENSE: Dynamic MRI with high frame rate exploiting spatiotemporal correlations. *Magnetic Resonance in Medicine*, 50:1031–1042, 2003.
- [40] B. Madore, G. H. Glover, and N. J. Pelc. Unaliasing by fourier-encoding the overlaps using the temporal dimension (UNFOLD), applied to cardiac imaging and fMRI. *Magnetic Resonance in Medicine*, 42:813–828, 1999.
- [41] K.P. Pruessmann, M. Weiger, M. B. Scheidegger, and P. Boesiger. SENSE: Sensitivity encoding for fast MRI. *Magnetic Resonance in Medicine*, 42:952–962, 1999.
- [42] D. K. Sodickson and W. J. Manning. Simultaneous acquisition of spatial harmonics (SMASH): fast imaging with radiofrequency coil arrays. *Magnetic Resonance in Medicine*, 38:591–603, 1997.
- [43] E. Schneider and G. Glover. Rapid in vivo proton shimming. *Magnetic Resonance in Medicine*, 18:335–347, 1991.
- [44] J.A. Fessler and D.C. Noll. Regularized fieldmap estimation in MRI. In *IEEE International Symposium on Biomedical Imaging 2006*, pages 706–709, 2006.
- [45] M.W. Woolrich, B.D. Ripley, J.M. Brady, and S.M. Smith. Temporal autocorrelation in univariate linear modeling of fMRI data. *Journal of Magnetic Resonance Imaging*, 14:1370–1386, 2001.
- [46] D.C. Noll. A genetic algorithm for optimal design of spectrally selective k-space. In *ISMRM Ninth Scientific Meeting*, page 681, 2001.
- [47] M. A. Griswold, P. M. Jakob, M. Nittka, J. W. Goldfarb, and A. Haase. Partially parallel imaging with localized sensitivities (PILS). *Magnetic Resonance in Medicine*, 44:602–609, 2000.
- [48] R.M. Heidemann, M.A. Griswold, N. Seiberlich, G. Kruger, and S.A.R. Kannengiesser. Direct parallel image reconstructions for spiral trajectories using GRAPPA. *Magnetic Resonance in Medicine*, page in press, 2006.
- [49] N. Seiberlich, R.M. Heidemann, F.A. Breuer, M. Blaimer, M.A. Griswold, and P.M. Jakob. Pseudo-Cartesian GRAPPA reconstruction of undersampled non-Cartesian data. In *ISMRM Fourteenth Scientific Meeting*, page 2463, 2006.
- [50] V. Rasche, D. Holz, and R. Proksa. MR fluoroscopy using projection reconstruction multi-gradient-echo (prMGE) MRI. *Magnetic Resonance in Medicine*, 42:324–334, 1999.

- [51] H. Eggers and P. Boesiger. Iterative ΔB_0 and T_2^* correction for radial multi-gradient-echo imaging. In *ISMRM Tenth Scientific Meeting*, page 348, 2004.
- [52] H. Eggers, T. Schaeffter, B. Aldefeld, and P. Boesiger. Combined δB_0 and t_2^* correction for radial multi-gradient-echo imaging. In *ISMRM Ninth Scientific Meeting*, page 478, 2003.
- [53] B.P. Sutton, D.C. Noll, and J.A. Fessler. Dynamic field map estimation using a spiral-in/spiral-out acquisition. *Magnetic Resonance in Medicine*, 51:1194–1204, 2004.
- [54] M. Barth, J.R. Reichenbach, R.Venkatesan, E. Moser, and E.M. Haacke. High-resolution, multiple gradient-echo functional MRI at 1.5T. *Magnetic Resonance Imaging*, 17:321–329, 1999.
- [55] G. H. Glover, S. K. Lemieux, M. Drangova, and J. M. Pauly. Decomposition of inflow and blood oxygen level-dependent (BOLD) effects with dual-echo spiral gradient-recalled echo (GRE) fMRI. *Magnetic Resonance in Medicine*, 35:299–308, 1996.
- [56] O. Speck and J. Hennig. Functional imaging by I_0 - and T_2^* -parameter mapping using multi-image EPI. *Magnetic Resonance in Medicine*, 40:243–248, 1998.
- [57] C. Schwarzbauer and W. Heinke. Investigating the dependence of bold contrast on oxidative metabolism. *Magnetic Resonance in Medicine*, "41":537–543", "1999".
- [58] A. B. Wennerberg, T. Jonsson, H. Forssberg, and T. Li. A comparative fmri study: T_2^* -weighted imaging versus R_2^* mapping. *NMR in Biomedicine*, 14:41–47, 2001.
- [59] D.B. Twieg. Parsing local signal evolution directly from a single-shot MRI signal: A new approach for fMRI. *Magnetic Resonance in Medicine*, 50:1043–1052, 2003.
- [60] V.T. Olafsson, D.C. Noll, and J.A. Fessler. New approach for estimating dR_2^* in fMRI. In *ISMRM Ninth Scientific Meeting*, page 132, 2003.
- [61] Lee S., Noll D.C., and Fessler J.A. EXTended Rosette ACquisition technique (EXTRACT): A dynamic R_2^* mapping method using extended rosette trajectory. In *ISMRM Tenth Scientific Meeting*, page 2128, 2004.
- [62] J. A. Fessler. Penalized weighted least-squares image reconstruction for positron emission tomography. *IEEE Transactions on Medical Imaging*, 13(2):290–300, 1994.
- [63] E. Schneider and G. Glover. Rapid in vivo proton shimming. *Magnetic Resonance in Medicine*, 18:335–347, 1991.
- [64] M.I. Altbach, A. Bilgin, Z. Li, E.W. Clarkson, and T.P. Trouard. Processing of radial fast spin-echo data for obtaining t_2 estimates from a single k-space data set. *Magnetic Resonance in Medicine*, 54:549–559, 2005.
- [65] J.A. Fessler and D.C. Noll. Iterative image reconstruction in MRI with separate magnitude and phase regularization. In *Proc. IEEE International Symposium on Biomedical Imaging*, page 209, 2004.
- [66] J.A. Fessler, S. Lee, V.T. Olafsson, H.R. Shi, and D.C. Noll. Toeplitz-based iterative image reconstruction for MRI with correction for magnetic field inhomogeneity. 53:3393–3402, 2005.
- [67] P. Jezzard, A. S. Barnett, and C. Pierpaoli. Characterization of and correction for eddy current artifacts in echo planar diffusion imaging. *Magnetic Resonance in Medicine*, 39:801–812, 1998.
- [68] S.M. Grieve, A.M. Blamire, and P. Styles. Elimination of nyquist ghosting caused by read-out of phase-encode gradient cross-terms in EPI. *Magnetic Resonance in Medicine*, 47:337–343, 2002.
- [69] J. H. Duyn, Y. Yang, J. A. Frank, and J. W. van der Veen. Simple correction method for k-space trajectory deviations in MRI. *Journal of Magnetic Resonance*, 132:150–153, 1998.

- [70] V.T. Olafsson, G.R. Lee, J.A. Fessler, and D.C. Noll. Interleaved spiral-in spiral-out 3D-FSE reconstruction using a fast field corrected iterative algorithm. In *ISMRM Thirteenth Scientific Meeting*, page 2298, 2005.
- [71] C.S. Law and G.H. Glover. Precompensation of spiral trajectory for reduced temporal fluctuation noise in fMRI. In *ISMRM Fourteenth Scientific Meeting*, page 3292, 2006.
- [72] Atsushi Takahashi and Terry Peters. Compensation of multi-dimensional selective excitation pulses using measured k-space trajectories. *Magnetic Resonance in Medicine*, 34:446–456, 1995.
- [73] N. G. Papadakis, A. A. Wilkinson, T. A. Carpenter, and L. D. Hall. A general method for measurement of the time integral of variant magnetic field gradients: Application to 2D spiral imaging. *Magnetic Resonance Imaging*, 15(5):567–578, 1997.
- [74] M. T. Alley, G. H. Glover, and N. J. Pelc. Gradinet characterization using a Fourier-transform technique. *Magnetic Resonance in Medicine*, 39:581–587, 1998.
- [75] G.F. Mason, T. Harshbarger, H. P. Hetherington, Y. Zhang, G. M. Pohost, and D. B. Twieg. A method to measure arbitrary k-space trajectories for rapid MR imaging. *Magnetic Resonance in Medicine*, 38:492–496, 1997.
- [76] D.J. Goodyear, M. Shea, S.D. Beyea, N.J. Shah, and B.J. Balcom. Single point measurements of magnetic field gradient waveform. *Journal of Magnetic Resonance*, 163:1–7, 2003.
- [77] G.H. Glover and C.S. Law. Spiral-in/out BOLD fMRI for increased SNR and reduced susceptibility artifacts. *Magnetic Resonance in Medicine*, 46:515–522, 2001.
- [78] R.H. Chan and M.K. Ng. Conjugate gradient methods for toeplitz systems. *SIAM review*, 38:427–482, 1996.
- [79] K. P. Pruessmann, M. Weiger, P. Börnert, and P. Boesiger. Advances in sensitivity encoding with arbitrary k-space trajectories. *Magnetic Resonance in Medicine*, 46:638–651, 2001.
- [80] C. T. W. Moonen and P. A. Bandettini, editors. *Functional MRI*. Springer-Verlag, Berlin, 1999.
- [81] Z. Wang, J. Wang, T.J. Connick, G.S. Wetmore, and J.A. Detre. Continuous ASL (CASL) perfusion MRI with an array coil and parallel imaging at 3T. *Magnetic Resonance in Medicine*, 54:732–737, 2005.

ABSTRACT

Iterative reconstruction methods for rosette trajectories in functional MRI

by

Sangwoo Lee

Chairs: Douglas Noll and Jeffrey Fessler

Blood Oxygenation Level Dependent (BOLD) functional MRI (Magnetic Resonance Imaging) is a noninvasive imaging method to explore the function of the human brain using the change of tissue T_2^* as the contrast mechanism. Fast imaging of the whole brain volume is important in fMRI, since the brain function can be spread over the entire brain for a very simple task. Simultaneous Multislice Acquisition using Rosette Trajectory (SMART) was proposed as one of the fast multislice imaging methods, but the non-iterative conjugate phase (CP) reconstruction resulted significant amount of artifacts from the off-resonance slices. In this thesis, we develop a physics model based iterative reconstruction method for SMART (iSMART) to reduce the artifacts and demonstrated the method at 3T. Simulation studies and functional experiments were performed to show that the method reduces most of the artifacts at the price of slight decrease in the in-plane spatial resolution and increased computation. The accuracy of iSMART depends on the accuracy of the system model it uses in the reconstruction. To increase the accuracy of the system model, we also developed

a robust, dynamic R_2^* -and-field-map-corrected image reconstruction method. This method is based on the spatio-temporally regularized iterative reconstruction algorithm. The spatio-temporally regularized iterative reconstruction estimates not only provides accurate field maps, but also field-map corrected images and the R_2^* map. Therefore, the spatio-temporally regularized iterative reconstruction can be used for dynamic R_2^* mapping for functional MRI experiments, where dynamic R_2^* mapping has a few advantages over the conventional T_2^* weighted BOLD imaging. It also can be used as dynamic field-map corrected BOLD imaging method. In simulations, we show that the method can improve the accuracy of the field map from the initial guess of the field map. In functional experiments, we show evidence that the proposed method can dynamically estimate and correct for the field map changes during a functional study. Further improvement on the accuracy of the system model can be achieved by the proposed 2D k-space trajectory measurement method. It is well known that time-varying magnetic fields induce eddy currents, which can distort the designed gradient waveforms. The proposed k-space trajectory measurement method utilizes pencil excitation at several spatial locations, and it measures main field fluctuations and crosstalk between two gradient channels. It requires reasonable scan time, and does not require extra equipment such as surface coil or a point phantom. A phantom experiment in a 3T scanner shows that even with the vendor-provided eddy current correction, there is remaining uncorrected distortion in the gradient waveforms.